Tug-of-war between cortical and cytoplasmic forces shaping planar 4-cell stage embryos

Silvia Caballero-Mancebo[1], Daniel Gonzalez Suarez[1], Janet Chenevert[1], Sameh Ben-Aicha[2], Lydia Besnardeau[1], Alex McDougall[1] and Rémi Dumollard[1*]

[1]Laboratoire de Biologie du Développement de Villefranche-sur-Mer, Institut de la Mer de Villefranche-sur-Mer, Sorbonne Université, CNRS, 06230 Villefranche-sur-Mer, France.
[2]Institut de Biologie de Valrose, Université Côte-d'Azur, CNRS, 03108 Nice, France.

* Corresponding author: remi.dumollard@imev-mer.fr

ABSTRACT

Early embryonic cleavages often follow conserved geometric rules, resulting in species-specific cleavage patterns. How these rules are mechanistically implemented, however, varies widely across species and remains poorly understood. Here, using quantitative 3D live imaging, mechanical and biochemical manipulations, we dissect the mechanisms governing centrosomal complex (CC) migration and spindle orientation in ascidian 2-cell stage embryos to generate the characteristic planar, square 4-cell stage. We show that following the first mitotic division, CCs in the two blastomeres form at variable orientations relative to the mother spindle and progressively achieve parallel and coplanar alignment during interphase of the 2-cell stage. Final spindle orientation is established prior to nuclear envelope breakdown, contrasting with dynamic spindle reorientation reported in other systems.

Our analyses reveal that CC rotation is driven by forces acting on long astral microtubules and guided by an anisotropic, ER-rich cytoplasmic domain that surrounds the CCs. This ER domain correlates with a dense astral microtubule network, enabling length-dependent microtubule pulling that orients the CCs independently of cell shape. In parallel, dynein-mediated cortical pulling refines spindle tilt and maintains coplanarity. Together, these findings uncover a cell-cycle-regulated tug-of-war between ER-mediated cytoplasmic forces and anisotropic cortical forces that ensures robust planar cleavage in ascidian early embryos.

INTRODUCTION

Species-specific patterns of early cleavage divisions have fascinated developmental biologists for more than a century. Despite the extraordinary diversity of embryo sizes and shapes, early cleavage planes typically follow two conserved geometric principles: Hertwig's rule, which states that the mitotic spindle aligns along the longest axis of the cell, highlighting the role of cell shape in dictating the orientation of the division plane[1,2] and the Sach's (or orthogonal) rule, where division occurs at right angles to the previous one[3], due to either centrosome chirality or cell shape. These rules collectively explain the widespread emergence of the planar, square arrangement of blastomeres at the 4-cell stage, a configuration observed across a broad spectrum of animal taxa, including cnidarians, echinoderms, ascidians, cephalochordates, and amphibians[4–6]. Yet, despite the apparent universality of these geometric rules, the mechanisms by which they are implemented are species-dependent and remain the subject of active investigation and debate.

In many species, the physical environment of the embryo—such as the presence of a rigid eggshell—can impose significant constraints on blastomere arrangement and cleavage orientation. For example, nematode embryos, encased in a rigid eggshell, display a striking diversity of 4-cell stage morphologies, ranging from square to linear configurations, depending on the mechanical properties and the aspect ratio of the eggshell[7–9]. In contrast, unconfined embryos and embryos with a non-restrictive confinement, such as ascidian and echinoderm embryos, more consistently exhibit the archetypal flat, square 4-cell configuration[10,11]. However, this configuration is far from the mechanically stable configuration of 4 blastomeres – a tetrahedron – but arises due to the short division times of early embryos[8], suggesting that oriented cell divisions underpin the flat and square shape of 4-cell stage embryos.

How spindle positioning is controlled during the first two cell divisions has been studied in many species and the picture so far is clouded by a diversity of behaviors between species of different embryonic size[12–14] and by remaining controversies in the canonical model, the *C. elegans* early embryo, where cytoplasmic pulling and cortical pulling or pushing have all been hypothesized to play a role in spindle orientation[15–18]. To generate a symmetric and flat 4-cell stage embryo, the first two cell divisions must be centered, equal, and at 90° to each other, and the mitotic spindles of each cell of the 2-cell stage embryo must be coplanar and parallel. One modelling approach suggests that geometric constraints coupled to either yolk stratification - as in *Xenopus* or ascidian embryos - or localized cortical factors - as in sea urchin embryos - are sufficient to generate flat 4-cell stage embryos[19]. A seducing part of this theory lies in its simplicity: pulling forces applied to astral microtubules must be proportional to their length[2,20]. Such force proportional to microtubule length is thought to be achieved by dynein-dependent pulling of cytoplasmic cargoes along their whole length. However, the nature of cytoplasmic cargoes remains to be established[19,21].

In smaller cells, cortical pulling forces become more prominent. In culture cells and cells of the *Drosophila* notum epithelium, cortical pulling forces have been shown to be essential in aligning the spindle with the long axis of the cell during interphase[22,23]. In *C. elegans* zygotes/embryos, one model predicts that cortical pulling can mediate alignment to the long axis of the zygote[16], whereas strong cortical pulling has also been shown to align spindles to the short axis of the AB cell in the 2-cell stage embryo before the actomyosin cytokinetic ring refines the alignment along the long axis[17]. A stochiometric theoretical model shows that there are more cortical pulling sites close to the

aster/spindle pole, and the forces generated at these sites result in the off-centering and alignment of the spindle with the short axis of the cell, thus having an opposing action to the length-dependent cytoplasmic pulling forces exerted on astral microtubules[17].

In ascidian embryos, centering cytoplasmic forces and off-centering cortical forces prevail during pronuclei migration in the zygote. Here, cortical pulling forces in the rear end of the sperm aster counteract cytoplasmic pulling forces generated at the front end[24]. In this study, we analyze the centrosome and spindle movements underlying the generation of a flat and square shape in ascidian 4-cell stage embryos. We find that centrosomal complexes (CCs) align progressively with the long length of the blastomeres during interphase when cortical pulling is strong. However, since we find that cortical pulling forces are reduced during mitosis, cortical pulling is likely to be dispensable for the rotation of the centrosomes that may instead rely on cytoplasmic pulling on the ER that is stratified in each cell of the 2-cell stage embryo. In line with this tug-of-war hypothesis, experimentally increasing cortical pulling, and thus interfering with the balance between cortical and cytoplasmic pulling forces, planar 4-cell stage embryos were transformed into non-planar embryos, highlighting that the balance between cytoplasmic and cortical pulling results in a dynamic "tug-of-war" that determines the cleavage pattern in early embryos.

RESULTS

Progressive coplanar and parallel alignment of the two centrosomal complexes at the 2-cell stage

In order to precisely follow the movements of the centrosomal complexes (CCs) during the 2-cell stage, we performed 3D live imaging of embryos injected with EB3-3xVenus to label the CCs from mitosis of 1-cell stage to the beginning of cytokinesis of the 2-cell stage (Fig. 1A, movie 1). In the vegetal view, two distinct centrosomes can be observed at each end of the spindle at anaphase of the 1-cell stage, coinciding with the beginning of cytokinesis of the first mitosis (Fig. 1A- inset, t = 2 min). We found that the CCs in the two forming daughter cells are not initially parallel to each other (in 60% of all analyzed embryos) and progressively align with each other during the interphase of the 2-cell stage, in contrast to *Xenopus* embryos, where the position of the centrosomes following the first mitosis determines the orientation of the spindle and the plane of division at the 2-cell stage[14]. This alignment results in two parallel CCs at nuclear envelope breakdown (NEBD) of the 2-cell stage (Fig. 1A, 16-20 min), which in turn give rise to two parallel spindles at metaphase of the 2-cell stage (Fig. 1A, 20-26 min). To generate the characteristic flat and square geometry of the ascidian 4-cell stage embryo, the two spindles at the 2-cell stage must not only be parallel but also coplanar. A side view (orthogonal to the vegetal view) revealed that, indeed, the two CCs remain largely coplanar throughout the 2-cell stage (Fig. 1A, bottom row).

To further document the complex migration pattern of CCs and how they orient over time, we tracked the position of the anterior and posterior centrosomes within each CC in 3D (Fig. 1B) and measured the rotation and tilt angles of each CC with respect to the mitotic spindle at 1-cell stage (Fig. 1C-D, S1A). We found that initially the CCs form with a rotation of 68.2° ± 24.6 with respect to the mother spindle, and that during interphase of the 2-cell stage, the CCs rotate to form a final angle of 82.5° ± 5.3 with respect to the mitotic spindle at the 1-cell stage by the time the daughter cells are in metaphase of the 2-cell stage. Surprisingly, this final position of the CCs does not change much from

134 the time of NEBD, contrary to what has been observed in other organisms and somatic cells, where
135 the final position of the spindle is fine-tuned during metaphase and anaphase[12,15,22], suggesting that
136 spindle positioning in ascidian embryos is largely predetermined before NEBD rather than dynamically
137 adjusted during mitosis.
138
139 Consistent with this idea, the tilt angle between the CCs and the 1-cell stage spindle also decreased
140 from 25.5° ± 22.4 to 15.1° ± 11.1 (Fig. 1D) but did not converge to zero, as would be expected for a flat
141 square 4-cell stage embryo. This observation is in agreement with previous reports describing a
142 posterior-vegetal tilt of the spindle in ascidians at the 8-cell stage[6]. Comparing the orientation of the
143 sister CCs and spindles at the 2-cell stage further confirmed our observations that they progressively
144 become parallel, as indicated by a reduction in the rotation angle between them from 48.4° ± 25 to
145 6.6° ± 5.5 (Fig. 1E, S1B - Rotation), and coplanar, as reflected by the decrease in the tilt angle between
146 them from 3.9° ± 4.8 to 1.8° ± 3.1 over time (Fig. 1E, S1B - Tilt). Altogether, this analysis revealed that
147 the proper orientation of the CCs required to generate a flat, square 4-cell stage ascidian embryo is
148 progressively established during the end of mitosis at 1-cell stage and interphase at 2-cell stage, and
149 that by the time of mitotic entry at 2-cell stage, the final position of the future spindle is already
150 defined.
151
152 To better understand the mechanisms that orient the CCs during the end of mitosis of the 1-cell stage
153 and interphase of the 2-cell stage, we examined their migration at a higher spatiotemporal resolution
154 (Fig. 2A, movie 2). We found that the CCs form in the center of the daughter cell at some distance from
155 the nucleus (~17 µm) before the first cleavage is complete (Fig. 2A, 30 s, arrowhead), and that the
156 centrosomes within each CC remain close to each other and move together until the end of interphase
157 of the 2-cell stage, when the centrosomes in each CC start to separate from each other and the nucleus
158 positions between them (Fig. 2A-B, 12- 14min) right before NEBD. Interestingly, the final orientation
159 of CCs is reached when the 2 centrosomes start separating (Fig. 1D-E, 2B) indicating that the rotation
160 of CCs occurs without separation of the centrosomes and suggesting that there is no need for Eg5
161 kinesin activity for CC rotation[25]. Since the centrosomes within a CC remain close together during their
162 migration, we asked whether a physical link between the 2 centrosomes is necessary for their proper
163 migration. To that end, we performed periodic laser ablations every 90 s between the two centrosomes
164 in one of the 2 sister CCs from the time when both centrosomes in each CC were identifiable (anaphase
165 of the 1-cell stage) until the nucleus reached the CC center (Fig. 2C, movie 3). We found that neither
166 rotation nor tilt was affected when centrosomes were ectopically separated by laser ablations (Fig.
167 2C', S2A-B), and that the ablated 2-cell stage embryos still divided into a flat and square 4-cell stage.
168 Because centrosome separation initiates when the nucleus reaches them, we assessed whether the
169 CCs use the nuclei to orient/power their movements as previously observed in *C. elegans* and
170 *Drosophila* embryo[15,26–28]. To test this possibility, we performed periodic laser ablations every 90 s
171 between the CC and the migrating nucleus in one of the two cells from the time both centrosomes in
172 the CC were identifiable until the nuclei reached the center of the CC (Fig. 2D, movie 4). We found that
173 these ablations could impair nucleus migration (Fig. S2C) but did not affect either CC migration or their
174 final orientation (Fig. 2D', S2D), as the CCs/spindles eventually became parallel and coplanar as in
175 control embryos.
176
177 Altogether these results show that CCs movements initiate at anaphase of mitosis I and proceed during
178 cytokinesis and interphase of the 2-cell stage in ascidians. These complex movements do not rely on

179 mechanisms previously described in other embryos such as *Xenopus* embryos[14], or *C. elegans* zygotes[26]
180 or *Drosophila* blastoderm embryos[27,29] and they are not supported by the nuclei or antiparallel
181 microtubules between centrosomes.
182
183 **CCs movements are powered by forces generated by astral microtubules**
184 As the abovementioned mechanisms do not appear to contribute to CC migration, we considered the
185 astral microtubule network as the most likely source of the forces driving CC migration. We first imaged
186 microtubule distribution at key times during CC migration and found that the network of astral
187 microtubules grows at anaphase of mitosis I and expands in the whole volume of the cell during
188 interphase before sharply retracting at prophase of the 2-cell stage (Fig. 3A). To understand how this
189 network remodeling could contribute to the migration of the CCs, we analyzed the density of
190 microtubules from the centrosome to the cell cortex. We found that in interphase (Fig. 3A'), a dense
191 network of microtubules is formed extending from the centrosomes across the central cytoplasm (Fig.
192 3A', blue shaded area), surrounded by a less dense peripheral network of microtubules near the cortex
193 (Fig. 3A', red shaded area). Upon mitotic entry, this organization was lost, and the microtubule network
194 became largely restricted to the pericentrosomal region, with the peripheral population markedly
195 diminished. (Fig. 3A''). The long astral microtubules observed during interphase may be the sites of
196 force generation to move CCs either by cytoplasmic pulling, as demonstrated in sea urchin embryos[2],
197 or by pulling of astral microtubules on the cell cortex previously shown in ascidian zygotes[24]. To test
198 this hypothesis, we performed periodic laser ablations of the astral microtubules (every 90 s) in one of
199 the 2 sister cells (Fig. 3B, movie 5) from the time when both centrosomes in each CC were identifiable
200 (anaphase of the 1-cell stage, 2 min) until NEBD of the 2-cell stage (17 min). We found that rotation of
201 the CCs was severely affected in the ablated cell but not in the non-ablated one (Fig. 3B'), and that the
202 sister CCs/spindles at the 2-cell stage were no longer parallel (Fig. S3A – Rotation Ablated). In contrast,
203 the tilt was not affected by these laser ablations (Fig 3B') and the CCs and spindles remained coplanar
204 (Fig. S3A – Tilt Ablated). To confirm these observations, we interfered with astral microtubules with 2-
205 methoxyestradiol (2ME), known to preferentially affect dynamic microtubules without impairing
206 spindle formation[30]. Incubating zygotes at anaphase of the 1-cell stage with 2ME drastically reduced
207 the size of centrosomal asters during interphase of the 2-cell stage (Fig. 3C) and prevented CC
208 migration, leading to strong defects in both rotation and tilt angles of the spindles at the end of 2-cell
209 stage, losing their coplanarity (Fig. 3C'-D, S3B-C).
210
211 Altogether, these results demonstrate that forces exerted on astral microtubules are responsible for
212 the proper migration and orientation of CCs/spindles in 2-cell stage ascidian embryos. In other
213 systems, such forces are generated by dynein motors through two main mechanisms: cortical pulling
214 forces, produced by dynein motors anchored at the plasma membrane that exert tension on astral
215 microtubules as they move toward their minus ends[22,31–33], and cytoplasmic pulling forces, generated
216 by dynein motors bound to intracellular organelles such as endoplasmic reticulum or endosomes[34–36].
217 To explore the contribution of these mechanisms to the shaping of planar ascidian 4-cell stage
218 embryos, we sought to localize intracellular dynein by immunocytochemistry against the dynein
219 localizing complex dynactin. Using ascidian-specific anti-dynactin antibody (see Materials and
220 Methods, Fig. 3E, S3D), we found that dynactin is enriched both in the pericentrosomal cytoplasm and
221 at the cell cortex. These two pools of dynactin closely correlate with the dense central and the
222 peripheral microtubule populations, respectively, observed in interphase cells (Fig. 3A').
223

224 Together, these findings suggest that dynein–dynactin complexes are enriched on locations supporting
225 a role for both cytoplasmic and cortical pulling in the positioning CCs and spindles. We then sought to
226 discriminate the role of each mechanism in the positioning of the CCs.
227
228 **An anisotropic ER domain may drive CC movements in the ascidian embryo.**
229 We first investigated the cytoplasmic source of force generation. Previous work has shown that the
230 cytoplasm of ascidian embryos is a dense mixture of yolk granules and organelles[37] and that the
231 interaction between cytoskeletal structures and cytoplasmic components generates forces that shape
232 the embryo and drive cytoplasmic organizations[38]. Moreover, recent studies have suggested that
233 astral microtubules are anchored to the endoplasmic reticulum (ER) of the cells via dynein motors and
234 are able to generate pulling and pushing forces, allowing spindles to orient (ref Salle/Minc/Levy).
235 Because yolk granules in ascidians do not accumulate around the sperm aster, as does the endoplasmic
236 reticulum and, to a lesser extent, the mitochondria of the myoplasm[24], we hypothesize that neither
237 the yolk nor the mitochondria display dynein motors anchored to their surface. We then asked if the
238 ER could serve as the guiding cue for the CCs and spindles to orient. First, we analyzed the distribution
239 of ER over time and found that from mitosis of the 1-cell stage, the spindle and the CCs were
240 surrounded by a cloud of ER (Fig. 4A, S4A, movie 6), closely resembling the pericentrosomal dense
241 astral microtubule population and the localization of dynactin (Fig. 3A, E and S4A). Segmentation and
242 morphometric analysis of the ER associated with the spindle and CCs revealed that, unlike the roughly
243 spherical shape of the cell-averaging 0.85 ± 0.05 sphericity during interphase, the ER forms a
244 cytoplasmic domain with an ellipsoid shape - 0.62 ± 0.04 sphericity - and a clearly defined long axis
245 (Fig. 4B).
246
247 The observed enrichment of microtubules, dynactin, and ER suggests that the ER is covered by dynein
248 motors and thus could be pulled when the ER interacts with astral microtubules. If this were the case,
249 the CCs could leverage this anisotropic ER domain to align with its long axis, as predicted by length-
250 dependent pulling on microtubule to position asters and spindles[39], even in the absence of a
251 geometrically defined long axis of the cell. To address this hypothesis, we quantified the relative
252 alignment between the long axes of the ER domain and the cell, and the CCs/spindles using bootstrap
253 statistics (Fig. 4C). We found that initially, the long axis of the cell, ER, and the CCs are not aligned to
254 each other (Fig. 4C – 2 min, 4D – 2 min), displaying random orientations which results in an average
255 angle of ~45° between the pairs. As cytokinesis and interphase progress, the angle between the long
256 axes of ER and the CCs/spindle gradually decreases, indicating progressive alignment before becoming
257 parallel at the end of interphase (Fig. 4C – 12 min, green; 4D – 12 min, green and grey). In contrast,
258 neither the long axis of the ER domain nor the CCs seem to align with the long axis of the cell over the
259 same period (Fig. 4C), suggesting that cell shape does not provide a dominant cue for spindle
260 orientation. Interestingly, at NEBD, which coincides with the shortening of the astral microtubules, the
261 ER and the forming spindle become momentarily misaligned (Fig. 4C – 17 min, 4D – 17 min), before
262 realigning with the cell axis at the onset of cytokinesis. Together, this analysis shows that the shape of
263 the cell may not provide a consistent geometrical cue for CC orientation, and suggests that, instead,
264 the ER acts as a cytoplasmic scaffold that guides spindle alignment independently of cell geometry,
265 even though the spindles obey the Hertwig rule[39].
266
267 Even though the shape of the 2-cell stage blastomeres remained fairly spherical, there may still be an
268 effect of cell shape in the positioning of the CCs and spindles. To further test whether the ER–spindle

269 alignment depends on external cell geometry or arises intrinsically from cytoplasmic organization, we
270 cultured the embryos in calcium and magnesium-free seawater (CMF) to remove the contribution of
271 cell adhesion (Fig. 4E-G, movie 7). The blastomeres of these embryos were almost perfectly spherical,
272 displaying an average sphericity of 0.96 ± 0.04, and still divided as control ones. The rotation angle
273 between the 2-cell stage CCs relative to the 1-cell spindle, however, was significantly altered, whereas
274 the tilt angle remained unaffected (Fig. 4E'–E''). The delayed rotation of the CCs at the end of the 2-
275 cell stage prevented the mitotic spindles from being parallel at mitosis (Fig. S4B-C), affecting the
276 characteristic square geometry of 4-cell stage embryos and suggesting that cell shape has an
277 instructive role in CC orientation. Nevertheless, the resulting 4-cell stage embryos in CMF remained
278 planar due to the CCs and spindles being coplanar during the whole CC migration (Fig. S4B-C). We then
279 analyzed the shape of the ER domain around CCs and spindles in CMF-cultured embryos, we observed
280 that the ER domain was also less ellipsoidal than in control embryos - average sphericity of 0.91 ± 0.04
281 - supporting the idea that the ER can serve as a proxy for cell shape by reinforcing the cell shape
282 anisotropy. When we compared the alignment dynamics between the ER domain and CCs in CMF
283 embryos, we found that absolute angles were consistently higher than in control embryos, indicating
284 reduced alignment between the ER and the CCs until mitosis of the 2-cell stage when the CCs and ER
285 align together (Fig. 4H). This suggests that cell geometry primarily impacts the progressive alignment
286 of CCs through rotation by cytoplasmic-generated forces, whereas the tilt angle does not seem to be
287 influenced by cell shape.
288
289 **Anisotropic cortical pulling forces maintains the CCs coplanar during CCs migration**
290 Given the established role of cortical pulling forces in spindle orientation across metazoans, and the
291 cortical localization of dynactin we observed (Fig. 3E), we next asked if cortical pulling forces control
292 the observed posterior tilt along the anterior-posterior axis we observe.
293
294 To that end, we first monitored the evolution of cortical pulling forces during CC migration by imaging
295 plasma membrane invaginations after cortical softening with 1 µg/ml Latrunculin B (Fig. 5A-A', movie
296 8)[24,40]. We found that plasma membrane invaginations appear at anaphase of the 1-cell stage and that
297 their frequency increases significantly during interphase of the 2-cell stage before sharply decreasing
298 at prophase and metaphase of the 2-cell stage mitosis (Fig. 5A''). These observations show a good
299 correlation between the appearance of the network of long astral microtubules and the occurrence of
300 cortical pulling, supporting the idea that cortical pulling may also be responsible for CC movements.
301 We then looked at the spatial distribution of cortical pulling sites and found that membrane
302 invaginations were more frequent at the posterior pole of the embryo compared to the anterior pole
303 (Fig. S5A) and that this difference was consistent throughout the migration of the CCs and persisted
304 until anaphase at the 2-cell stage. These findings support our observations of a posterior tilt of the CCs
305 and spindles along the anterior–posterior axis (Fig. 1C, E) and suggest that asymmetrical cortical pulling
306 forces may play a central role in regulating the tilt angle and coplanarity of CCs and spindles, thereby
307 maintaining the planar architecture of the 4-cell stage embryo. Surprisingly, analysis of CCs and spindle
308 orientation in Latrunculin B-treated embryos (Fig. S5B) showed that neither rotation nor tilt angles are
309 affected by drastic softening of the embryo cortex (Fig. S5B') and that the spindles at mitosis of the
310 putative 2-cell stage remain parallel and coplanar (Fig. S5B''). These observations align with previous
311 reports that reducing actomyosin contractility has minimal impact on sperm aster positioning in
312 ascidian zygotes[24] or early spindle orientation[17], and are consistent with studies showing that cortical

313 pulling can persist when actin integrity is compromised[41], while excessive cortical tension can suppress
314 pulling[42]. Thus, the question remains as to whether cortical pulling can regulate CCs movements.
315
316 The observation of the posterior bias in cortical pulling forces and its correlation with spindle tilt led
317 us to hypothesize that cortical pulling forces actively control centrosome orientation and that
318 increasing cortical pulling would affect CCs orientation[17] by amplifying spindle tilt which would perturb
319 the coplanarity of the 4-cell stage embryos. In animal cells, cortical pulling forces are mediated by
320 dynein–NuMA–LGN–Gαi complexes anchored to the plasma membrane[22]. In this complex, the
321 heterotrimeric G-protein subunit Gαi recruits LGN to the cortex, which in turn binds NuMA. NuMA
322 then acts as a scaffold linking the cortical complex to astral microtubules, thereby positioning dynein
323 motors to generate pulling forces as they move toward the microtubule minus ends, generating
324 tension from the cortex to astral microtubules and enabling dynein to pull centrosomes and spindles
325 toward specific cortical regions. To test whether increasing cortical pulling alters CCs/spindle
326 positioning and embryo geometry, we overexpressed NuMA and targeted it to the cortex by fusing it
327 to a pleckstrin homology (PH) domain, which promotes membrane localization. In embryos expressing
328 PH-NuMA, the fusion protein predominantly accumulated at the posterior cortex (Fig. 5B, bottom row,
329 0 min; movie 9). The cortical pulling assay in these embryos confirmed a global increase in the number
330 of plasma membrane invaginations (Fig. 5B', Total) compared to control embryos (Fig. 5A''), with a
331 higher frequency of posterior pulling sites, confirming that cortical pulling was strengthened and
332 correlated with the accumulation of PH-NuMA.
333
334 Analysis of the orientation of CCs/spindles in embryos overexpressing cortical NuMA showed a larger
335 tilt angle at the 2-cell stage relative to the spindle at the 1-cell stage, while rotation remained largely
336 unaffected (Fig. 5C-C'', S5D, movie 10). The increased tilt was also reflected in the higher tilt angle
337 between sister spindles at the 2-cell stage (Fig. S5C, S5D - Tilt) that were not coplanar, resulting in
338 embryos adopting a more tetrahedral configuration (Fig. 5C, 26 min), in contrast to the planar
339 geometry observed in controls. Altogether, these results suggest a model in which proper spindle
340 orientation and maintenance of the planar 4-cell embryo geometry depend on a finely tuned tug-of-
341 war between cortical and cytoplasmic dynein-mediated pulling forces acting on astral microtubules in
342 a cell cycle-dependent manner (Fig. 5D).
343
344
345 **DISCUSSION**
346 Our study uncovers the mechanisms that drive the dynamic centrosomal complex (CC) migration and
347 spindle orientation in early ascidian embryos and identifies a previously underappreciated balance
348 between cortical and cytoplasmic forces as a key determinant of embryo geometry. Through
349 quantitative live imaging, perturbation assays, and biophysical manipulations, we reveal that ascidian
350 embryos rely on a finely tuned interplay — a tug-of-war — between dynein-dependent forces acting
351 from the cell cortex and those acting from cytoplasmic interactions that are most likely transmitted
352 through the endoplasmic reticulum (ER) network to achieve the characteristic planar 4-cell stage
353 configuration.
354
355 Our data provide a comprehensive analysis of the dynamic behavior and mechanisms underlying
356 centrosomal complex (CC) and spindle positioning in 2-cell stage ascidian embryos. We demonstrate
357 that the CCs of the two cells at 2-cell stage initially form at varying angles relative to the position of the

first mitotic spindle and progressively achieve parallel alignment during interphase of the 2-cell stage. This progressive alignment is essential for the formation of the characteristic square 4-cell stage ascidian embryo. Interestingly, our study revealed a second cue that drives the coplanarity of the CCs, ensuring the planar arrangement of the blastomeres at 4-cell stage.

Previous studies in other model organisms have indicated that final spindle orientation is adjusted during mitosis[15,17,22,42]. Notably, our data reveal that in ascidian 2-cell stage embryos, the final orientation of the CCs and the spindle is established before mitotic entry and remains largely unchanged during subsequent mitosis. Our findings reinforce the notion that precise spindle orientation is a critical determinant for embryonic patterning and morphogenesis. The progressive coplanar and parallel alignment of CCs ensures that the resulting 4-cell stage embryo adopts the correct geometry, which is a prerequisite for subsequent morphogenetic events and fate determination in ascidian embryos. Interestingly, the tilt angle between the CCs and the mother spindle does not converge to zero, consistent with previous reports of a posterior-vegetal tilt in ascidian spindles at later stages[6]. Nevertheless, the tilt angle between the CCs/spindles at 2-cell stage is close to zero, essential for the flat, square shape of the 4-cell stage.

Our results highlight both conserved and divergent mechanisms of spindle orientation across metazoans. In well-studied systems such as *C. elegans*, *Drosophila*, and *Xenopus* embryos, spindle orientation is often dynamically regulated by a combination of cortical pulling forces, nuclear positioning, and microtubule-based mechanisms[26–29]. In these organisms, the mitotic spindle can continue to rotate and adjust its orientation well into mitosis, and dynein-mediated cortical pulling and antiparallel microtubule sliding are critical for proper centrosome positioning[16,17]. In contrast, our laser ablation experiments in ascidian embryos reveal that neither the integrity of the CCs nor the migration of the nucleus is required for the final orientation of the CCs and spindles. Disruption of centrosome separation or nuclear migration does not perturb the progressive alignment of the CCs, nor does it affect the ability of embryos to divide into flat, square 4-cell stage embryos. This finding suggests that ascidian embryos employ a distinct mechanism for spindle orientation that is largely independent of the nuclear or centrosomal cues that are crucial in other systems.

The discovery that the ER serves as a proxy for cell shape and guides spindle orientation in ascidian embryos has significant implications for the understanding of force generation and spatial organization during early development. It suggests that organelle-based cues can play a dominant role in orchestrating the orientation of cell division by generating cytoplasmic forces that are sufficient to maintain directional coupling, yet whose efficiency depends on geometric constraints imposed by cell–cell contacts. Moreover, the ER-rich domain that forms around the spindle—arising from the local mutual exclusion of both ER sheets and yolk granules—underscores the crucial role that cytoplasmic reorganizations and stratification have in early in development. The spatial organization of the endoplasmic reticulum provides experimental evidence that a stratified cytoplasm can shape where and how intracellular forces are generated and transmitted, which in turn influences spindle behavior[19]. The persistence of planar (but not square) divisions in CMF seawater further implies that cortical inputs primarily refine coplanarity, while ER-based cytoplasmic forces provide the dominant contribution to CC rotation and global spindle alignment.

Together, these findings support a model in which the positioning of CCs and spindles arises from the integration of two mechanically distinct dynein-driven systems (Fig. 5D). Cytoplasmic pulling forces, transmitted through ER–microtubule coupling, act as a global aligning mechanism that orients the CCs along a cytoplasmic long axis. In contrast, cortical pulling forces, mediated by the dynein–NuMA–LGN complex, provide localized tension that fine-tunes spindle tilt and ensures coplanarity of the embryo. Proper spindle orientation thus depends on a delicate balance: cytoplasmic forces define the overall orientation, whereas cortical forces adjust and stabilize the geometry relative to the embryo's boundaries. Perturbing either component — by weakening microtubule dynamics, increasing cortical pulling, or removing cell shape constraints — disrupts this balance and results in aberrant, non-planar cleavage patterns.

Our findings expand the repertoire of known mechanisms by which cells can achieve precise spatial organization during development and highlight the evolutionary diversity of strategies employed by different organisms. Proper spindle orientation is not only critical for ensuring correct cleavage patterns and cell fate specification but also for the establishment of tissue architecture and organogenesis. The mechanisms uncovered in ascidian embryos may thus inform our understanding of how similar processes are regulated in other organisms, and may provide insights into the evolution of developmental strategies across metazoans.

ACKNOWLEDGEMENTS

We would like to thank Hervé Turlier for fruitful discussions and the Microscopy Imaging Platform (PIM) and the animal facility (CRB) of the Institut de la Mer de Villefranche (IMEV) for their continuous support. This work was supported by a Joint Project Grant from the FWF (I 3601-B27).

AUTHORS CONTRIBUTIONS

S.C.-M., A.M., and R.D. designed the research. S.C.-M. performed the experiments and analyzed the experimental data. D.G.S. contributed to the data analysis. J.C. performed the immunostainings and antibody validations. S.C.-M. and S.B-A. performed the laser ablation experiments. L.B. created the pSPE3-EB3-mScarlet, pSPE3-Reticulon-Venus, and pSPE3-PH-NuMA-Venus constructs. S.C.-M. and R.D. wrote the manuscript.

FUNDING

The project was funded by the Agence Nationale de la Recherche grants ''MorCell'' (ANR-17-CE 13-0028) and "InvBlastula" (ANR-22-CE13-0036-01)

DATA AVAILABILITY

All relevant data can be found within the article and its supplementary information. All other data supporting the findings of this study are available from the corresponding author on request.

447 **REFERENCES**

448 1. Hertwig, O. *Das Problem der Befruchtung und der Isotropie des Eies: eine Theorie der Vererbung*.
449 (Verlag von Gustav Fischer, 1884).
450 2. Minc, N., Burgess, D. & Chang, F. Influence of Cell Geometry on Division-Plane Positioning. *Cell*
451 144, 414–426 (2011).
452 3. Sachs, J. *Über Die Anordnung Der Zellen in Jüngsten Pflanzentheilen*. (Druck und Verlag der
453 Stahel'schen Buch- & Kunsthandlung, 1877).
454 4. Caballero-Mancebo, S. *et al.* Marine model organisms for mechanobiology studies. in *Evo-Devo: In*
455 *Search of New Model Species* (Springer-Nature, 2026).
456 5. McDougall, A., Chenevert, J., Godard, B. G. & Dumollard, R. Emergence of Embryo Shape During
457 Cleavage Divisions. in *Evo-Devo: Non-model Species in Cell and Developmental Biology* (eds
458 Tworzydlo, W. & Bilinski, S. M.) 127–154 (Springer International Publishing, Cham, 2019).
459 doi:10.1007/978-3-030-23459-1_6.
460 6. Negishi, T., Takada, T., Kawai, N. & Nishida, H. Localized PEM mRNA and Protein Are Involved in
461 Cleavage-Plane Orientation and Unequal Cell Divisions in Ascidians. *Curr. Biol.* 17, 1014–1025
462 (2007).
463 7. Schulze, J. & Schierenberg, E. Evolution of embryonic development in nematodes. *EvoDevo* 2, 18
464 (2011).
465 8. Giammona, J. & Campàs, O. Physical constraints on early blastomere packings. *PLoS Comput. Biol.*
466 17, e1007994 (2021).
467 9. Krenger, R., Burri, J. T., Lehnert, T., Nelson, B. J. & Gijs, M. A. M. Force microscopy of the
468 Caenorhabditis elegans embryonic eggshell. *Microsyst. Nanoeng.* 6, 29 (2020).
469 10. Minc, N. & Piel, M. Predicting division plane position and orientation. *Trends Cell Biol.* 22, 193–200
470 (2012).
471 11. Grill, S. W. & Hyman, A. A. Spindle Positioning by Cortical Pulling Forces. *Dev. Cell* 8, 461–465
472 (2005).
473 12. Gönczy, P., Grill, S., Stelzer, E. H., Kirkham, M. & Hyman, A. A. Spindle positioning during the
474 asymmetric first cell division of Caenorhabditis elegans embryos. *Novartis Found. Symp.* 237, 164–
475 175; discussion 176-181 (2001).
476 13. Wu, H., Nazockdast, E., Shelley, M. J. & Needleman, D. J. Forces positioning the mitotic spindle:
477 Theories, and now experiments. *BioEssays* 39, 1600212 (2017).
478 14. Wühr, M., Tan, E. S., Parker, S. K., Detrich, H. W. & Mitchison, T. J. A model for cleavage plane
479 determination in early amphibian and fish embryos. *Curr. Biol. CB* 20, 2040–2045 (2010).
480 15. Bondaz, A., Cirillo, L., Meraldi, P. & Gotta, M. Cell polarity–dependent centrosome separation in
481 the C. elegans embryo. *J. Cell Biol.* 218, 4112–4126 (2019).
482 16. Wu, H.-Y. *et al.* Laser ablation and fluid flows reveal the mechanism behind spindle and
483 centrosome positioning. *Nat. Phys.* (2023).
484 17. Middelkoop, T. C. *et al.* A cytokinetic ring-driven cell rotation achieves Hertwig's rule in early
485 development. *Proc. Natl. Acad. Sci.* 121, e2318838121 (2024).
486 18. Kimura, K. & Kimura, A. Intracellular organelles mediate cytoplasmic pulling force for centrosome
487 centration in the Caenorhabditis elegans early embryo. *Proc. Natl. Acad. Sci. U. S. A.* 108, 137–142
488 (2011).
489 19. Pierre, A., Sallé, J., Wühr, M. & Minc, N. Generic Theoretical Models to Predict Division Patterns of
490 Cleaving Embryos. *Dev. Cell* 39, 667–682 (2016).

20. Kimura, K. & Kimura, A. A novel mechanism of microtubule length-dependent force to pull centrosomes toward the cell center. *BioArchitecture* 1, 74–79 (2011).
21. Xie, J. *et al.* Contribution of cytoplasm viscoelastic properties to mitotic spindle positioning. *Proc. Natl. Acad. Sci.* 119, e2115593119 (2022).
22. Anjur-Dietrich, M. I. *et al.* Mechanics of spindle orientation in human mitotic cells is determined by pulling forces on astral microtubules and clustering of cortical dynein. *Dev. Cell* (2024).
23. Unified quantitative characterization of epithelial tissue development | eLife. https://elifesciences.org/articles/08519.
24. Rosfelter, A. *et al.* Reduction of cortical pulling at mitotic entry facilitates aster centration. *J. Cell Sci.* 137, jcs262037 (2024).
25. Yu, W.-X. *et al.* Kinesin-5 Eg5 is essential for spindle assembly, chromosome stability and organogenesis in development. *Cell Death Discov.* 8, 490 (2022).
26. Meyerzon, M. *et al.* Centrosome attachment to the C. elegans male pronucleus is dependent on the surface area of the nuclear envelope. *Dev. Biol.* 327, 433–446 (2009).
27. Buttrick, G. J. *et al.* Akt regulates centrosome migration and spindle orientation in the early Drosophila melanogaster embryo. *J. Cell Biol.* 180, 537–548 (2008).
28. Tanenbaum, M. E. & Medema, R. H. Mechanisms of Centrosome Separation and Bipolar Spindle Assembly. *Dev. Cell* 19, 797–806 (2010).
29. Wong, S.-S., Wainman, A., Saurya, S. & Raff, J. W. Regulation of centrosome size by the cell-cycle oscillator in Drosophila embryos. *EMBO J.* 43, 414–436 (2024).
30. Kamath, K. *et al.* 2-Methoxyestradiol suppresses microtubule dynamics and arrests mitosis without depolymerizing microtubules. *Mol. Cancer Ther.* 5, 2225–2233 (2006).
31. Laan, L. *et al.* Cortical Dynein Controls Microtubule Dynamics to Generate Pulling Forces that Reliably Position Microtubule Asters. *Cell* 148, 502–514 (2012).
32. Kiyomitsu, T. The cortical force-generating machinery: how cortical spindle-pulling forces are generated. *Curr. Opin. Cell Biol.* 60, 1–8 (2019).
33. Omer, S., Greenberg, S. R. & Lee, W.-L. Cortical dynein pulling mechanism is regulated by differentially targeted attachment molecule Num1. *eLife* 7, e36745 (2018).
34. Stefano, G., Renna, L. & Brandizzi, F. The endoplasmic reticulum exerts control over organelle streaming during cell expansion. *J. Cell Sci.* 127, 947–953 (2014).
35. Woźniak, M. J. *et al.* Role of kinesin-1 and cytoplasmic dynein in endoplasmic reticulum movement in VERO cells. *J. Cell Sci.* 122, 1979–1989 (2009).
36. Shamipour, S., Caballero-Mancebo, S. & Heisenberg, C.-P. Cytoplasm's Got Moves. *Dev. Cell* 56, 213–226 (2021).
37. Stoev, I. D. *et al.* Active and Probe-Free Intracellular Rheology via Phase-Sensitive Thermoviscous Flows. 2025.04.07.647540 Preprint at https://doi.org/10.1101/2025.04.07.647540 (2025).
38. Caballero-Mancebo, S. *et al.* Friction forces determine cytoplasmic reorganization and shape changes of ascidian oocytes upon fertilization. *Nat. Phys.* 20, 310–321 (2024).
39. Dumollard, R. *et al.* The invariant cleavage pattern displayed by ascidian embryos depends on spindle positioning along the cell's longest axis in the apical plane and relies on asynchronous cell divisions. *eLife* 6, e19290 (2017).
40. Godard, B. G., Dumollard, R., Heisenberg, C.-P. & McDougall, A. Combined effect of cell geometry and polarity domains determines the orientation of unequal division. *eLife* 10, e75639 (2021).
41. Redemann, S. *et al.* Membrane Invaginations Reveal Cortical Sites that Pull on Mitotic Spindles in One-Cell C. elegans Embryos. *PLOS ONE* 5, e12301 (2010).

42. Kelkar, M. *et al.* Spindle reorientation in response to mechanical stress is an emergent property of the spindle positioning mechanisms. *Proc. Natl. Acad. Sci.* 119, e2121868119 (2022).

MATERIALS AND METHODS

Biological material

Adult *Phallusia mammillata* were collected in Sète (France) and kept at 16 °C in the aquaria of the Centre de Resources Biologiques (CRB) of the Institut de la Mer de Villefranche (IMEV) which is an EMBRC-France certified service (https://www.embrc-france.fr/fr/nos-services/fourniture-de-ressources-biologiques/organismes-modeles/ascidie-phallusia-mammillata). All experiments were performed at 18-19 °C. Oocytes and sperm were obtained after animal dissection and were used on the day of collection. Oocytes were chemically dechorionated in a 0.1 % trypsin solution (Sigma-Aldrich, T8003) in micro-filtered natural sea water (MFSW; Nalgene 0.2 µm filters, cat. no. Z370584) for 90 min under gentle stirring and kept in until fertilization with 6 µl sperm that was activated by resuspension in 1 ml of MSFW at pH 9.2.

Embryos were cultured either in MFSW or in Ca2+ and Mg2+-free sea water (CMF) supplemented with 1 mM EDTA[43].

Cloning of expression constructs

To generate the pSPE3-EB3-mScarlet plasmid, the EB3 coding sequence was amplified from pRN3-EB3-3xVenus vector using the following primers with EcoRI and XhoI sites, respectively: 5'-GAATTCAAAATGGCCGTCAATGTGTACTCCACAT-3' and 5'-CTCGAGGTACTCGTCCTGGTCTTCTTGTTGA-3'. The mScarlet coding sequence (including stop codon) was amplified from the plasmid pSPE3-iMyo-mScarlet[38] using the following primers with XhoI and NotI sites, respectively: 5'-CTCGAGATGGTGAGCAAGGGCGAGGCAGTG-3' and 5'-GCGGCCGCCTACTTGTACAGCTCGTCCATGCC-3'. To generate the pSPE3-EB3-mScarlet plasmid, the PCR products were ligated into a pSPE3-Rfa destination vector that had been previously digested with EcoRI and NotI.

To generate the pSPE3-Reticulon-Venus plasmid, the reticulon coding sequence was amplified using the following primers: 5'-CACCATGGAGTATGAAACGAGCCC-3' and 5'-CTCTGCTTTAGGCTTGGCACC-3'. The PCR product was used to generate an entry vector using the pDONR/TOPO (p3M-Reticulon). The entry vector was recombined with the destination vector pSPE3-Rfa-Venus.

To generate the pSPE3-PH-NuMA-Venus plasmid, the PH and NuMA coding sequences were amplified using hybridizing primers as follows: 5'-AAGCAGGCTCCGCGGCCGCCCCCTTCA-3' and 5'-GAGCTCAACATCATGGATGATGACGAAA-3' for PH and 5'-GAGCTCAACATCATGGATGATGACGAAA-3' and 5'-GTCTGAATCCAAAAAAGAAGGGTGGGCG-3' for NuMA. After hybridization, the full PH-NuMA coding sequence was amplified using the following primers: 5'-ACAAGTTTGTACAAAAAAGCAGGCTCCGCGGCCGCCCCCTTCA-3' and 5'-GTCTGAATCCAAAAAAGAAGGGTGGGCGCGCCGACCCAGCTTTCTTGTACAAAGTGGT-3'. The final PCR product was used to generate an entry vector using the pDONR/TOPO (p3M-PH-NuMA). The entry vector was recombined with the destination vector pSPE3-Rfa-Venus[44].

579 *mRNA microinjections*
580 Microinjections were performed as described[45]. Microinjection needles (Harvard Apparatus, 30-
581 0035) were pulled with a PN-30 puller (Narishige) and mounted on a micromanipulation setup
582 (MMO-203, Narishige) attached to an Olympus IX70 microscope. Dechorionated unfertilized eggs
583 were placed into a glass wedge mounted onto a 400 µl Perspex mounting chamber (see for
584 detailed protocol McDougall et al., 2014). *In vitro* mRNA synthesis was performed using the
585 mMESSAGE mMACHINE T3 Transcription Kit 562 (Ambion, AM1343). The following mRNAs were
586 injected: EB3-Venus[24], EB3-mScarlet (this study), Ensconsin-3xGFP[46], Ensconsin-dTomato[46], H2B-
587 Venus[47], PH-dTomato[47], PH-NuMA-Venus (this study), and Reticulon-Venus (this study). mRNAs
588 were injected at a concentration of 2-4 µg/µl using a high-pressure system (Narishige IM300) and
589 incubated at 16 °C overnight before the experiment.
590
591 *Myoplasm and plasma membrane labeling*
592 Dechorionated unfertilized oocytes or zygotes were incubated in a 1 µM solution of MitoTracker™
593 Deep Red FM (Thermo Fisher, M22426) to label the myoplasm and/or in a 1 µM solution of
594 CellMask™ Orange (Thermo Fisher, C10045) in MFSW for 5 min and washed in MFSW before
595 imaging.
596
597 *Cytoskeletal inhibitors*
598 To soften the cortex, 1 µg/ml Latrunculin B (Sigma-Aldrich, L5288) was added to the imaging dish 40
599 minutes post fertilization (right before first cell division) and left in the medium for the remainder of
600 the experiment.
601 To interfere with dynamic microtubules, 1 µg/ml 2-methoxyestradiol (Merck, 362-07-2) was added to
602 the imaging dish 40 minutes post fertilization (right before first cell division) and left in the medium for
603 the remainder of the experiment.
604
605 *Confocal live imaging*
606 Embryos were mounted 40 minutes post fertilization in glass bottom dishes (Cellvis, D35-10-0-N)
607 coated with 1% low melting point agarose (Thermo Fisher, 16500100) in MFSW. Embryos were imaged
608 in either an inverted Leica TCS SP8 confocal microscope or an inverted Leica Stellaris confocal
609 microscope using a HCPL APO CS2 40x/1.1 NA water immersion objective (Leica) and Hybrid detectors.
610 Embryos were imaged *in toto* with an optical section thickness of 3 µm every 120-180 s. For membrane
611 invagination experiments, the frame rate was reduced to 30 s and for fixed samples, the optical section
612 was 1 µm.
613
614 *Laser ablation*
615 Embryos were mounted 40 minutes post fertilization as for confocal live imaging and imaged on a Zeiss
616 LSM980 confocal microscope equipped with a two-photon pulsed laser using a C-Aprochromat 40x/1.1
617 NA water immersion objective. Microtubules between centrosomes or between centrosomes and the
618 nucleus were cut along a 10 µm line and astral microtubules were cut along 50 µm lines in 3 z planes,
619 all of which were performed with a two-photon Coheren Axon 920-2 laser (2.5W). For ablation, the
620 two-photon laser was used at full power, and the power received at the focal point is estimated at 2.8
621 $\cdot 10^{12}$ W/m^2. Embryos were imaged over 50 central z-slices with an optical section thickness of 1 µm
622 every 13 s.

623 *Antibody production*
624 The anti-dynactin mouse polyclonal antibody was produced by fusing 1002 base pairs, amino acids 35
625 to 334, of the *Ciona intestinalis* dynactin subunit 1 protein (GenBank AP042712.1) to a 6-His tag at the
626 C terminus and cloned into the vector pET11. Expression in bacteria was induced with IPTG, and the
627 dynactin fusion protein was purified on a nickel column and eluted with imidazole according to the
628 manufacturer (Potrino Ni-NTA column, Macherey-Nagel). Immunization of mice was performed by
629 Covalab (France), and sera obtained after 57 days were used directly without further purification.
630
631 *Immunostaining*
632 Embryos were fixed in 100% methanol (VWR Chemicals, 67-56-1), which had been pre-chilled at −20°C,
633 and then stored at -20°C. Samples were rehydrated by three washes in PBS containing 0.1% Tween
634 (PBS-Tw), then blocked in PBS-Tw containing 1% BSA for 1 hour at room temperature. Primary
635 antibodies to tyrosinated alpha tubulin (rat anti-alpha-tubulin tyrosinated, monoclonal YL1/2, Merck,
636 MAB1864-I) or to dynactin subunit 1 (mouse polyclonal, custom made, see above) were added at a
637 dilution of 1/500 in blocking buffer and incubated for at least 24 hours at 4 °C. After incubation,
638 samples were washed three times in PBS-Tw, and fluorescent anti-rat (Jackson ImmunoResearch) or
639 anti-mouse secondary antibodies (Jackson ImmunoResearch) were added at a dilution of 1/200. After
640 further incubation at room temperature for 1-2 hours, samples were washed in PBS-Tw, labelled with
641 Hoechst 33342 (final concentration 5 µg/ml, Thermo Fisher, 23491-52-3) for 10 minutes, washed twice
642 more in PBS-Tw, and mounted on glass slides in CitiFluor AF1 (Electron Microscopy Services, 17970-
643 25). To prevent embryo compression or breakage, coverslips were elevated by application of small
644 spacers of modelling clay at the corners as described (ref).
645
646 *Western blot*
647 Anti-dynactin antibody's specificity was validated by Western blot analysis showing a single band at
648 ~55 kDa corresponding to dynactin (Fig. S3D).
649 2 and 8-cell stage embryos were collected in a small volume of MFSW and mixed with the same volume
650 of 2x Laemmli sample buffer (100 mM Tris-HCL pH 6.8, 4% SDS, 0.2% Bromophenol Blue, 20% glycerol
651 and 200 mM dithiothreitol). Samples were heated for 5 min at 95 °C and then stored at -20 °C. Proteins
652 were separated by electrophoresis on SDS-polyacrylamide gels and transferred to a nitrocellulose
653 membrane. Membranes were stained briefly with Ponceau-S, then washed with TBS-Tw (20 mM Tris
654 Base and 150 mM NaCl plus 0.1% Tween-20), and blocked for at least 1 hour in TBS-Tw containing 5%
655 dry milk powder. Immunoblots were then incubated in anti-dynactin primary antibody diluted 1:1000
656 overnight at 4 °C. Membranes were then washed three times with TBS-Tw and incubated with an anti-
657 mouse horseradish peroxidase-conjugated secondary antibody (Jackson ImmunoResearch, 115-035-
658 003) at 1:10,000 dilution in TBS-Tw + 5% dry milk powder for 2 hours at room temperature. After three
659 washes in TBS-Tw, signal detection was carried out using the SuperSignal™ West PLUS Pico
660 chemiluminescent substrate (ThermoFisher Scientific, 34580) and images were acquired with a Fusion
661 FX system (Vilber Lourmat, Collegien, France).
662
663 *3D tracking of centrosomes and angle quantification*
664 Confocal fluorescent Z-stacks of embryos injected with EB3-3xVenus and PH-dTomato were stabilized
665 using the MultiStackReg[48] plugin in Fiji[49]. Centrosomes were then tracked using the MTrackJ[50] plugin
666 in Fiji, and their 3D coordinates (Ci_x, Ci_y, Ci_z) were used to calculate the polar angles (rotation and
667 tilt) with the y-axis (embryonic anterior-posterior axis) as reference.

Centrosome separation

The 3D coordinates of each centrosome were used to calculate the distance between each centrosome within a CC: d = $\sqrt{(C1_x - C2_x)^2 + \left(C1_y - C2_y\right)^2 + (C1_z - C2_z)^2}$

Distance between nucleus and CC

Confocal fluorescent Z-stacks of embryos injected with H2B-Venus and EB3-mScarlet were stabilized using MultiStackReg plugin in Fiji. Centrosomes were then tracked using the MTrackJ plugin in Fiji and their 3D coordinates (Ci_x, Ci_y, Ci_z) used to calculate the midpoint of the CC, $M_{CC} = \left(\frac{C1_x + C2_x}{2}, \frac{C1_y + C2_y}{2}, \frac{C1_z + C2_z}{2}\right)$. The nucleus of each cell was segmented and tracked using the Surface tool in Imaris (Bitplane). Then the distance at every time point between the nucleus (Ni_x, Ni_y, Ni_z) and the CC midpoint was calculated: $d = \sqrt{(M_x - N_x)^2 + \left(M_y - N_y\right)^2 + (M_z - N_z)^2}$. The radius of the nucleus was subtracted from the distance to reflect the time when the edge of the nucleus reaches the center of the CC.

Microtubules intensity profile

The intensity profiles of microtubules were made using the line tool of 15-pixel thickness in Fiji from the centrosome to the plasma membrane. The intensity values shown were normalized to the maximum intensity value along each line. The distance between the centrosome and the plasma membrane was also normalized.

Membrane invagination quantification

Confocal fluorescent Z-stacks of embryos incubated in CellMask™ Orange to label the plasma membrane were stabilized using MultiStackReg plugin in Fiji. 10 confocal z-slides over the equator of the embryo were sum projected. The number of membrane invaginations was counted manually by counting the invaginations present at 2-10 µm from the plasma membrane[24] at the times indicated in Fig. 5A' and B.

Endoplasmic Reticulum segmentation

Confocal fluorescent Z-stacks of embryos injected with either Reticulon-Venus and PH-dTomato, Reticulon-Venus and Ensconsin-dTomato or Reticulon-Venus and EB3-mScarlet were stabilized using the MultiStackReg plugin in Fiji. For segmentation a Gaussian filter (sigma = 2) was applied and segmented using Ilastik software[51] and the pixel classification method.

Plasma membrane segmentation

Confocal fluorescent Z-stacks of embryos injected with PH-dTomato were stabilized using the MultiStackReg plugin in Fiji and segmented using Cellpose[52].

Shape analysis

Principal component analysis (PCA) of segmented membrane and ER timelapses was performed in order to obtain the direction of the 3 main axes using a custom-made Python script. To compute the length of the main axes (a, b, c), each voxel from the segmented images was projected onto each axis, and sphericity was calculated as: $sphericity = \sqrt[3]{c^2/ab}$.

Data analysis and statistics

Statistical analysis was performed using Prism 8 (GraphPad). The statistical test used in each case and the resulting P values are indicated in each figure legend. N was considered an independent experiment, and n denotes the number of cells; N and n are indicated in each figure. No statistical method was used to predetermine sample size. The experiments were not randomized.

METHODS-SPECIFIC REFERENCES

43. Sardet, C. *et al.* Embryological Methods in Ascidians: The Villefranche-sur-Mer Protocols. in *Vertebrate Embryogenesis: Embryological, Cellular, and Genetic Methods* (ed. Pelegri, F. J.) 365–400 (Humana Press, Totowa, NJ, 2011). doi:10.1007/978-1-61779-210-6_14.
44. Roure, A. *et al.* A Multicassette Gateway Vector Set for High Throughput and Comparative Analyses in Ciona and Vertebrate Embryos. *PLOS ONE* 2, e916 (2007).
45. McDougall, A., Lee, K. W.-M. & Dumollard, R. Microinjection and 4D fluorescence imaging in the eggs and embryos of the ascidian Phallusia mammillata. *Methods Mol. Biol. Clifton NJ* 1128, 175–185 (2014).
46. Costache, V. *et al.* Kif2 localizes to a subdomain of cortical endoplasmic reticulum that drives asymmetric spindle position. *Nat. Commun.* 8, 917 (2017).
47. Prodon, F. *et al.* Dual mechanism controls asymmetric spindle position in ascidian germ cell precursors. *Development* 137, 2011–2021 (2010).
48. Thevenaz, P., Ruttimann, U. E. & Unser, M. A pyramid approach to subpixel registration based on intensity. *IEEE Trans. Image Process.* 7, 27–41 (1998).
49. Schindelin, J. *et al.* Fiji: an open-source platform for biological-image analysis. *Nat. Methods* 9, 676–682 (2012).
50. Meijering, E., Dzyubachyk, O. & Smal, I. Methods for Cell and Particle Tracking. in *Methods in Enzymology* vol. 504 183–200 (Elsevier, 2012).
51. Berg, S. *et al.* ilastik: interactive machine learning for (bio)image analysis. *Nat. Methods* 16, 1226–1232 (2019).
52. Stringer, C., Wang, T., Michaelos, M. & Pachitariu, M. Cellpose: a generalist algorithm for cellular segmentation. *Nat. Methods* 18, 100–106 (2021).

FIGURES

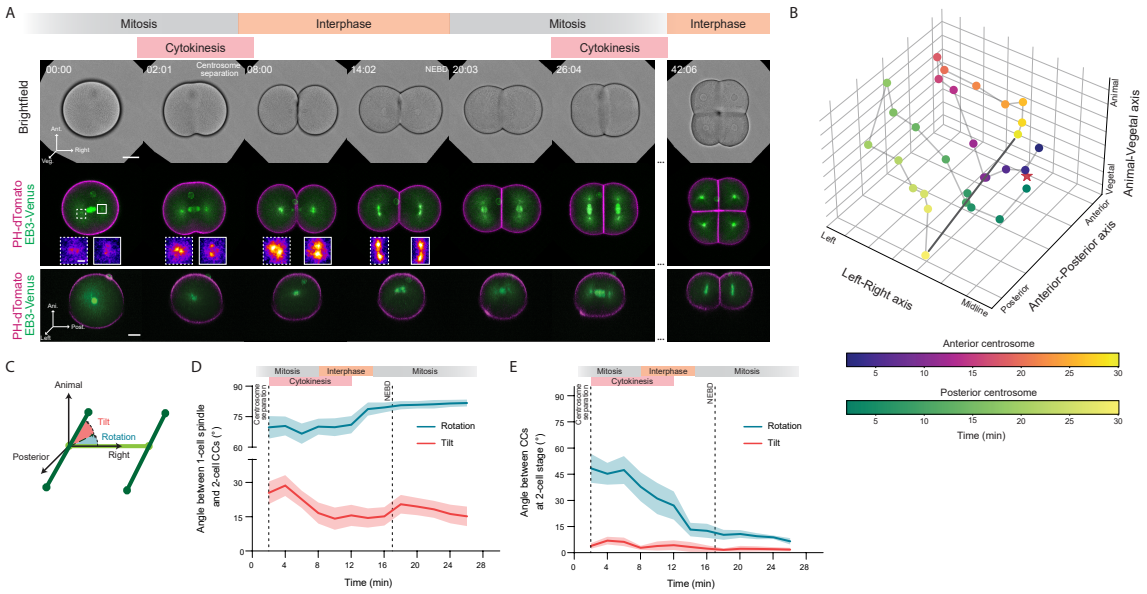

Figure 1: The two CCs become parallel and coplanar during interphase of the 2-cell stage.
(A) Brightfield, confocal fluorescent images of a central z-slide of the plasma membrane (magenta), and maximum intensity projections of centrosomes (green) in a representative ascidian embryo from 1-cell stage metaphase (time = 00:00) to 4-cell stage interphase (time = 40:05). The top and middle rows show the vegetal view, and the bottom row shows the side view. Insets are high magnifications of the left (dashed square) and right (solid square) CCs. Ant. is anterior, Veg. is vegetal, Ani. is animal, Post. is posterior, and NEBD is nuclear envelope breakdown. Time is in minutes:seconds. Scale bar, 30 µm. Inset scale bar, 5 µm.
(B) Example of a 3D plot of the relative positions over time of the anterior and posterior centrosomes of the CC in the left cell of a 2-cell stage ascidian embryo. Time is coded in the respective color bar for each centrosome. The star represents the position of the left centrosome of the mitotic spindle at 1-cell stage, and the grey line represents the final orientation of the spindle at mitosis of the 2-cell stage.
(C) Graphical representation of the tilt and rotation angles between the CCs and the spindles at the 2-cell stage (dark green) and the spindle at the 1-cell stage (light green). Embryonic axes are shown for reference.
(D) Plot of the rotation (blue) and tilt (red) angles between the CCs and the spindle at 2-cell stage and the spindle at 1-cell stage as a function of time after centrosome separation (2 min, dashed vertical line). The dashed line at 17 min indicates the time of NEBD. *N* = 9 embryos, *n* = 18 cells. Error bars, standard error of the mean (s.e.m.).
(E) Plot of the rotation (blue) and tilt (red) angles between the left and right CCs and spindles at 2-cell stage as a function of time after centrosome separation (2 min, dashed vertical line). The dashed line at 17 min indicates the time of NEBD. *N* = 9 embryos. Error bars, standard error of the mean (s.e.m.).

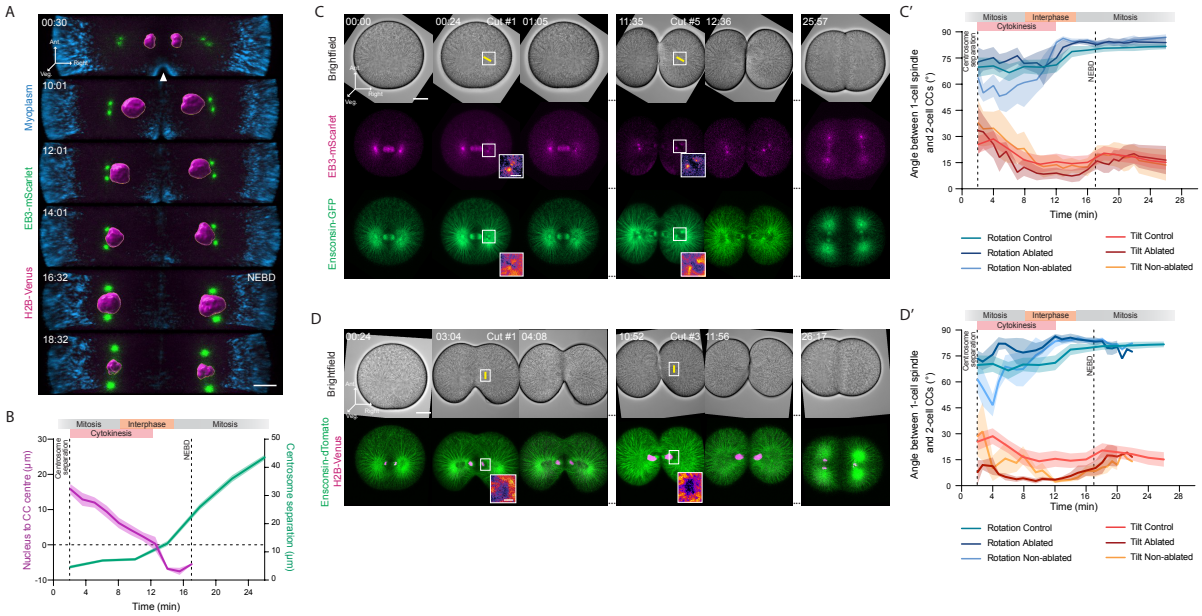

Figure 2: Migration of the CCs and nucleus during interphase of the 2-cell stage.

(A) Confocal maximum intensity projections of the centrosomes (green), mitochondria (cyan), and segmented nuclei (magenta) in a representative ascidian embryo during interphase of the 2-cell stage. Ant. is anterior, Veg. is vegetal, and NEBD is nuclear envelope breakdown. Arrowhead demarcates the ingressing cytokinetic furrow. Time is in minutes:seconds. Scale bar, 10 µm

(B) Plot of the distance between the edge of the nucleus and the center of the CC (magenta, left *y* axis; *N* = 6 embryos, *n* = 12 cells) and the separation of the centrosomes within a CC (green, right *y* axis; *N* = 9 embryos, *n* = 18 cells) as a function of time after centrosome separation (2 min, dashed vertical line). The dashed line at 17 min indicates the time of NEBD. Error bars, standard error of the mean (s.e.m.).

(C) Brightfield and maximum intensity projections of confocal fluorescent images of centrosomes (magenta, middle row) and microtubules (green, bottom row) during laser ablation of microtubules between the centrosomes. The yellow line demarcates the ablation site. The square demarcates the area of the inset. Ant. is anterior, Veg. is vegetal. Time is in minutes:seconds. Scale bar, 30 µm. Inset scale bar, 5 µm.

(C') Plot of the rotation and tilt angles between the CCs and the spindle at 2-cell stage and the spindle at 1-cell stage as a function of time after centrosome separation (2 min, dashed vertical line) in control embryos (*N* = 9 embryos, *n* = 18 cells), ablated cell (*N* = 5 embryos, *n* = 5 cells), and non-ablated cell (*N* = 5 embryos, *n* = 5 cells) in laser-ablated embryos between the centrosomes. The dashed line at 17 min indicates the time of NEBD. Error bars, standard error of the mean (s.e.m.).

(D) Brightfield and maximum intensity projections of confocal fluorescent images of the DNA (magenta) and microtubules (green) during laser ablation of microtubules between the nucleus and the CC. The yellow line demarcates the ablation site. The square demarcates the area of the inset. Ant. is anterior, Veg. is vegetal. Time is in minutes:seconds. Scale bar, 30 µm. Inset scale bar, 5 µm.

(D') Plot of the rotation and tilt angles between the CCs and the spindle at 2-cell stage and the spindle at 1-cell stage as a function of time after centrosome separation (2 min, dashed vertical line) in control embryos (*N* = 9 embryos, *n* = 18 cells), ablated cell (*N* = 4 embryos, *n* = 4 cells), and non-ablated cell (*N* = 4 embryos, *n* = 4 cells) in laser-ablated embryos between the centrosomes and the nucleus. The dashed line at 17 min indicates the time of NEBD. Error bars, standard error of the mean (s.e.m.).

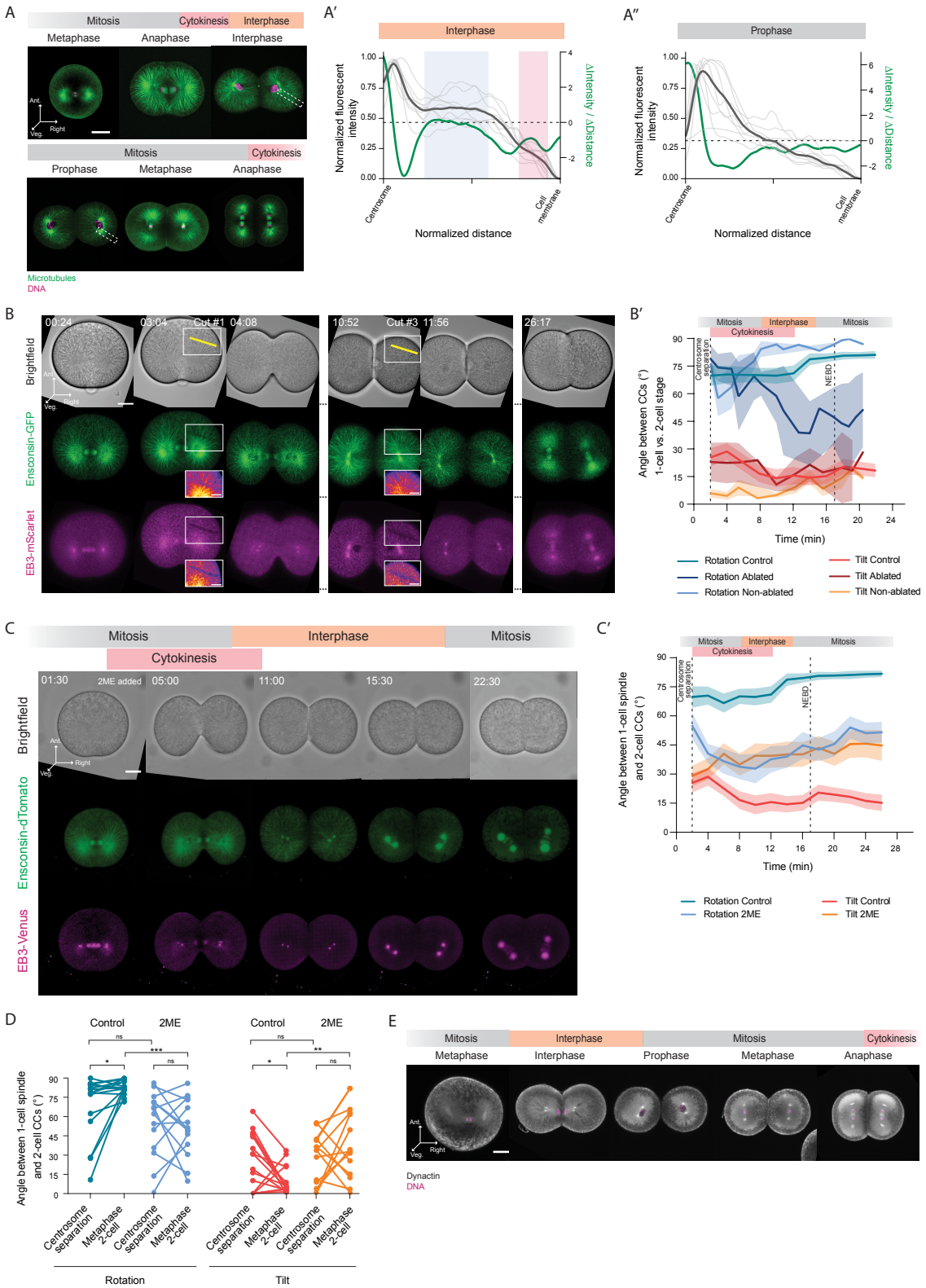

Figure 3: Forces generated along astral microtubules are essential for the orientation of CCs.
(A) Confocal images of a central z-slice of ascidian embryos from 1-cell stage metaphase to 2-cell stage anaphase stained for microtubules (green) and DNA (magenta). Ant. is anterior, Veg. is vegetal. The dashed area indicates the analyzed area in A' and A''. Scale bar, 40 µm.

(A’, A’’) Fluorescent intensity profiles show the distribution of microtubules from the centrosome to the cell membrane in embryos in interphase (left *y* axis; *N* = 9 embryos) and in prophase (left *y* axis; *N* = 8 embryos). The green line (right *y* axis) represents the change in the average intensity profile over the distance.

(B) Brightfield and maximum intensity projections of confocal fluorescent images of microtubules (green, middle row) and centrosomes (magenta, bottom row) during laser ablation of astral microtubules. The yellow line demarcates the ablation site. The square demarcates the area of the inset. Ant. is anterior, Veg. is vegetal. Time is in minutes:seconds. Scale bar, 30 µm. Inset scale bar, 20 µm.

(B’) Plot of the rotation and tilt angles between the CCs and the spindle at 2-cell stage and the spindle at 1-cell stage as a function of time after centrosome separation (2 min, dashed vertical line) in control embryos (*N* = 9 embryos, *n* = 18 cells), ablated cell (*N* = 4 embryos, *n* = 4 cells), and non-ablated cell (*N* = 4 embryos, *n* = 4 cells) in laser-ablated embryos. The dashed line at 17 min indicates the time of NEBD. Error bars, standard error of the mean (s.e.m.).

(C) Brightfield and maximum intensity projections of confocal fluorescent images of microtubules (green, middle row) and centrosomes (magenta, bottom row) in embryos treated with 1µg/ml 2-methoxyestradiol (2ME). Ant. is anterior, Veg. is vegetal. Time is in minutes:seconds. Scale bar, 30 µm.

(C’) Plot of the rotation and tilt angles between the CCs and the spindle at 2-cell stage and the spindle at 1-cell stage as a function of time after centrosome separation (2 min, dashed vertical line) in control embryos (*N* = 9 embryos, *n* = 18 cells) and embryos treated with 2ME (*N* = 7 embryos, *n* = 14 cells). The dashed line at 17 min indicates the time of NEBD. Error bars, standard error of the mean (s.e.m.).

(D) Plot of the initial (Centrosome separation) and final (Metaphase 2-cell) rotation (left) and tilt (right) angles between the CCs and the spindle at 2-cell stage with respect to the spindle at 1-cell stage in control embryos (*N* = 9 embryos, *n* = 18 cells; rotation: paired Wilcoxon test, *P=0.0131; tilt: paired Wilcoxon test, *P=0.0250) and embryos treated with 2-methoxyestradiol (*N* = 7 embryos, *n* = 14 cells; rotation and tilt: paired t test, ns - not significant). Control vs. 2ME rotation angle: Kruskal-Wallis test (***P=0.0001) with Dunn's multiple comparisons test (ns – not significant, ***P=0.0001). Control vs. 2ME tilt angle: Kruskal-Wallis test (*P=0.0101) with Dunn's multiple comparisons test (ns – not significant, **P<0.0025).

(E) Confocal images of a central z-slice of ascidian embryos from 1-cell stage metaphase to 2-cell stage anaphase stained for dynactin (grey) and DNA (magenta). Ant. is anterior, Veg. is vegetal. Scale bar, 30 µm.

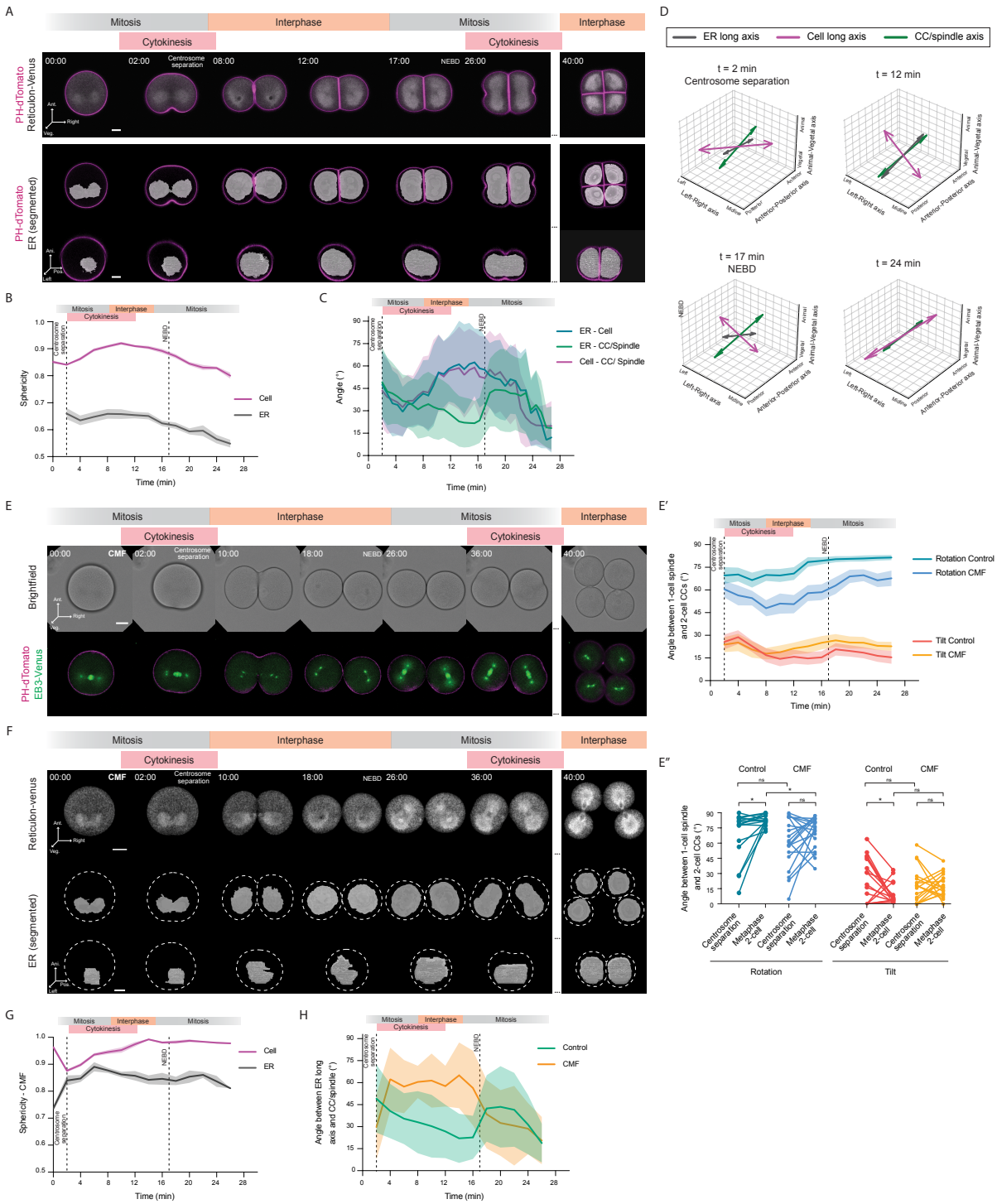

Figure 4: Cytoplasmic pulling controls the rotation of the CCs.

(A) Confocal fluorescent images of a central z-slice of the plasma membrane (magenta) and the endoplasmic reticulum (grey) in a representative ascidian embryo from 1-cell stage metaphase to 4-cell stage interphase. The middle and bottom rows show a top and side view, respectively, of the membrane (magenta) and the segmented ER (grey). Ant. is anterior, Veg. is vegetal, Ani. is animal, Post. is posterior, and NEBD is nuclear envelope breakdown. Time is in minutes:seconds. Scale bar, 30 µm.

869 **(B)** Plot of the sphericity of the cell (magenta; *N* = 14 embryos) and the ER (grey; *N* = 12 embryos) as a
870 function of time after centrosome separation (2 min, dashed vertical line) in control embryos. The
871 dashed line at 17 min indicates the time of NEBD. Error bars, standard error of the mean (s.e.m.).
872 **(C)** Plot of the angle between the long axis of the ER and the cell (blue), the long axis of the ER and the
873 CCs and spindle (green) and the long axis of the cell and the CCs and spindle (red) as a function of time
874 after centrosome separation (2 min, dashed vertical line) in control embryos. The dashed line at 17
875 min indicates the time of NEBD. Error bars, standard deviation (s.d.). Mean and s.d. were estimated by
876 bootstrap method (5000 iterations).
877 **(D)** 3D plots of the average long axis of the cell (magenta), the long axis of the ER (grey), and the CCs
878 and spindle (green) at 2, 12, 17, and 24 minutes of the left cells of ascidian embryos after metaphase
879 of the 1-cell stage. NEBD is nuclear envelope breakdown. For visualization purposes, the length of the
880 long axis of the cell (magenta) and the CCs (green) are doubled.
881 **(E)** Brightfield, confocal fluorescent images of a central z-slide of the plasma membrane (magenta),
882 and maximum intensity projections of centrosomes (green) in a representative ascidian embryo in Ca^{2+}
883 and Mg^{2+}-free sea water (CMF) from 1-cell stage metaphase to 4-cell stage interphase. Ant. is anterior,
884 Veg. is vegetal, Ani. is animal, Post. is posterior, and NEBD is nuclear envelope breakdown. Time is in
885 minutes:seconds. Scale bar, 40 µm.
886 **(E')** Plot of the rotation and tilt angles between the CCs and the spindle at 2-cell stage and the spindle
887 at 1-cell stage as a function of time after centrosome separation (2 min, dashed vertical line) in control
888 embryos (*N* = 9 embryos, *n* = 18 cells) and embryos in CMF (*N* = 10 embryos, *n* = 20 cells). The dashed
889 line at 17 min indicates the time of NEBD. Error bars, standard error of the mean (s.e.m.).
890 **(E'')** Plot of the initial (Centrosome separation) and final (Metaphase 2-cell) rotation (left) and tilt
891 (right) angles between the CCs and the spindle at 2-cell stage and the spindle at 1-cell stage in control
892 embryos (*N* = 9 embryos, *n* = 18 cells; rotation: paired Wilcoxon test, *P=0.0131; tilt: paired Wilcoxon
893 test, *P=0.0250) and embryos in CMF (*N* = 10 embryos, *n* = 20 cells; rotation and tilt: paired t test, ns -
894 not significant). Control vs. CMF rotation angle: Kruskal-Wallis test (*P=0.0194) with Dunn's multiple
895 comparisons test (ns – not significant, *P=0.0276). Control vs. CMF tilt angle: Kruskal-Wallis test (ns –
896 not significant) with Dunn's multiple comparisons test (ns – not significant).
897 **(F)** Confocal fluorescent images of the endoplasmic reticulum (top row) and its segmentation (middle
898 row is the top view and bottom row is the side view) in a representative ascidian embryo from 1-cell
899 stage metaphase to 4-cell stage interphase in CMF. Ant. is anterior, Veg. is vegetal, Ani. is animal, Post.
900 is posterior, and NEBD is nuclear envelope breakdown. Time is in minutes:seconds. Scale bar, 30 µm.
901 **(G)** Plot of the sphericity of the cell (magenta; *N* = 4 embryos) and the ER (grey; *N* = 10 embryos) as a
902 function of time after centrosome separation (2 min, dashed vertical line) in embryos incubated in CMF
903 sea water. The dashed line at 17 min indicates the time of NEBD. Error bars, standard error of the mean
904 (s.e.m.).
905 **(H)** Plot of the angle between the long axis of the ER and the CCs and spindle as a function of time after
906 centrosome separation (2 min, dashed vertical line) in control embryos (green, taken from C) and in
907 CMF-cultured embryos (orange). The dashed line at 17 min indicates the time of NEBD. Error bars,
908 standard deviation (s.d.).
909
910
911
912
913

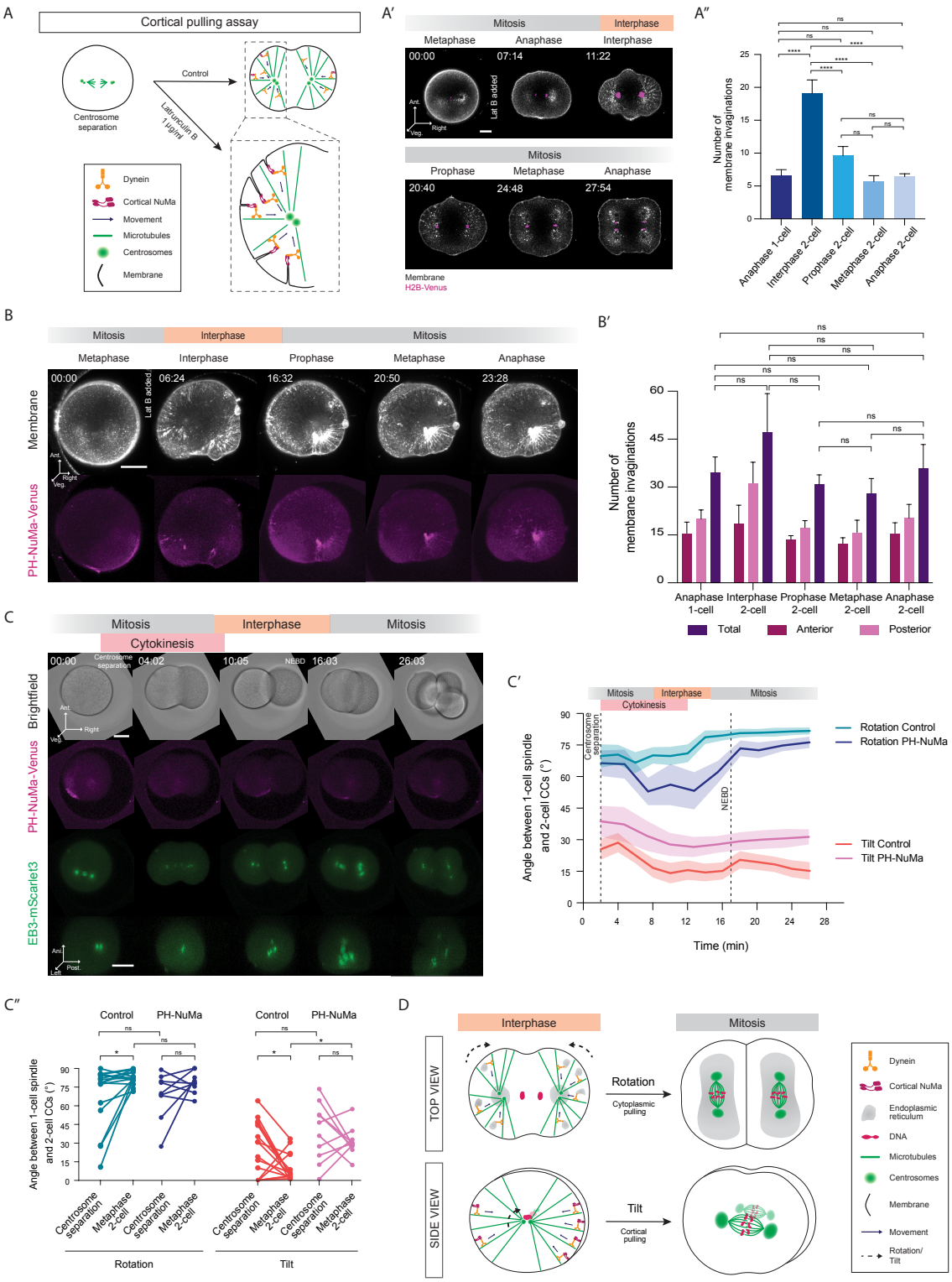

Figure 5: The tilt along the anterior-posterior axis is controlled by cortical pulling forces.

(A) Schematic representation of the cortical pulling assay to test the presence of cortical pulling sites by the formation of membrane invaginations towards the CCs in a soft-cortex ascidian embryo.

(A') Confocal maximum intensity projections over 6 central z-slices of the plasma membrane (grey) and DNA (magenta) in a representative ascidian embryo from 1-cell stage metaphase to 2-cell stage

922 anaphase, treated with 1µg/ml Latrunculin B from 1-cell stage anaphase. Ant. is anterior, Veg. is
923 vegetal. Time is in minutes:seconds. Scale bar, 30 µm.
924 **(A'')** Bar plot of the average number of membrane invaginations as a function of the cell cycle stage.
925 (*N* = 13 embryos). One-way ANOVA (****P<0.0001) and Tukey's multiple comparisons tests
926 (****P<0.0001; ns - not significant). Error bars, standard error of the mean (s.e.m.).
927 **(B)** Confocal maximum intensity projections over 6 central z-slices of PH-NuMA (magenta) and
928 membrane (grey) in ascidian embryos expressing PH-NuMA and treated with 1µg/ml Latrunculin B
929 from 1-cell stage anaphase. Scale bar, 40µm.
930 **(B')** Bar plot of the average number of membrane invaginations (anterior, posterior, and total) as a
931 function of the cell cycle stage in embryos expressing PH-NuMA and treated with 1µg/ml Latrunculin
932 B. (*N* = 4 embryos). Kruskal-Wallis test (ns – not significant) and Dunn's multiple comparisons tests (ns
933 - not significant). Error bars, standard error of the mean (s.e.m.).
934 **(C)** Brightfield and maximum intensity projections of confocal fluorescent images of PH-NuMA
935 (magenta) and centrosomes (green) in embryos expressing PH-NuMA. Ant. is anterior, Veg. is vegetal,
936 Ani. is animal, Post. Is posterior. Time is in minutes:seconds. Scale bar, 40 µm.
937 **(C')** Plot of the rotation and tilt angles between the CCs and the spindle at 2-cell stage and the spindle
938 at 1-cell stage as a function of time after centrosome separation (2 min, dashed vertical line) in control
939 embryos (*N* = 9 embryos, *n* = 18 cells) and embryos expressing PH-NuMA (*N* = 5 embryos, *n* = 10 cells).
940 The dashed line at 17 min indicates the time of NEBD. Error bars, standard error of the mean (s.e.m.).
941 **(C'')** Plot of the initial (Centrosome separation) and final (Metaphase 2-cell) rotation (left) and tilt
942 (right) angles between the CCs and the spindle at 2-cell stage and the spindle at 1-cell stage in control
943 embryos (*N* = 9 embryos, *n* = 18 cells; rotation: paired Wilcoxon test, *P=0.0131; tilt: paired Wilcoxon
944 test, *P=0.0250) and embryos expressing PH-NuMA (*N* = 7 embryos, *n* = 14 cells; rotation and tilt:
945 paired t test, ns - not significant). Control vs. PH-NuMA rotation angle: Kruskal-Wallis (*P=0.0201) with
946 Dunn's multiple comparisons test (ns – not significant). Control vs. PH-NuMA tilt angle: Kruskal-Wallis
947 (**P=0.0073) with Dunn's multiple comparisons test (ns – not significant, *P=0.0169).
948 **(D)** Schematic model of the two mechanisms controlling the positioning of the CCs during the 2-cell
949 stage: cytoplasmic dynein-dependent pulling along astral microtubules controls the 90°C rotation of
950 the CCs with respect to the 1-cell stage mitotic spindle. Dynein motors on the surface of the ER are
951 pulled towards the CCs, thus forming the pericentromeric ER domains. These domains, in turn, act as
952 a proxy for cell shape, dictating the rotation of the CCs during interphase to generate a square 4-cell
953 stage embryo. Concomitantly with cytoplasmic pulling, cortical dynein generates cortical pulling forces
954 at the end of astral microtubules that control the tilt of the CCs, ensuring the coplanarity of sister CCs
955 and the planar geometry of the 4-cell stage ascidian embryo.
956
957
958
959
960
961
962
963
964

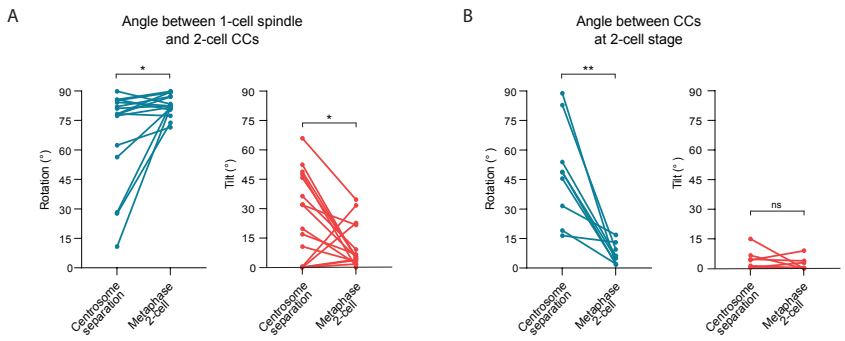

Figure S1: CCs of sister cells become parallel and coplanar at the 2-cell stage (relative to Fig. 1). **(A)** Plot of the initial (Centrosome separation) and final (Metaphase 2-cell) rotation (left) and tilt (right) angles between the CCs and the spindle at 2-cell stage and the spindle at 1-cell stage (*N* = 9 embryos, *n* = 18 cells; rotation: paired Wilcoxon test, *P=0.0131; tilt: paired Wilcoxon test, *P=0.0250). **(B)** Plot of the initial (Centrosome separation) and final (Metaphase 2-cell) rotation (left) and tilt (right) angles between he left and right CCs and spindles at 2-cell stage (*N* = 9 embryos; rotation: paired t test, **P=0.0017; tilt: paired Wilcoxon test, ns – not significant).

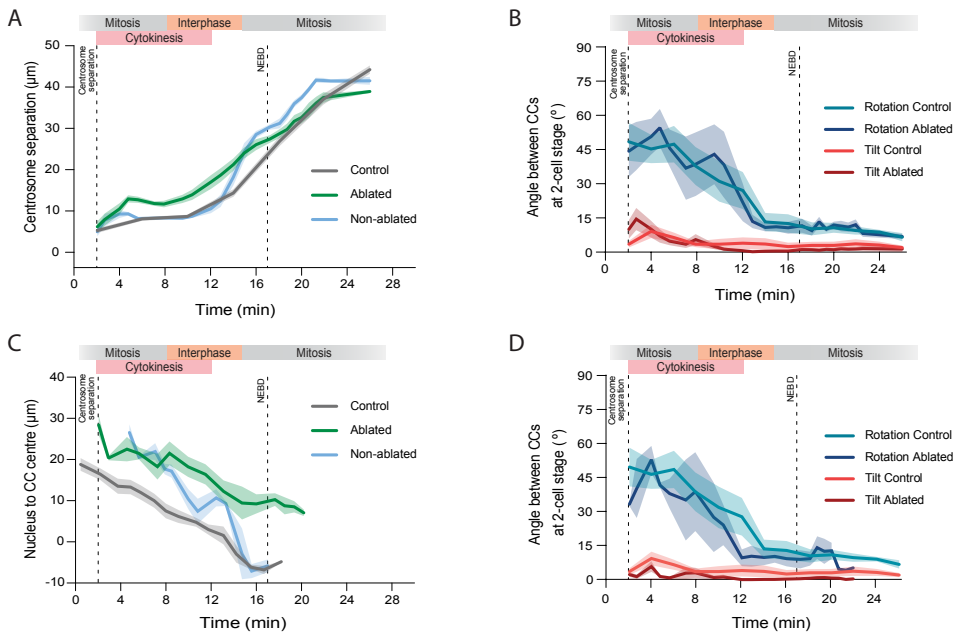

Figure S2: Centrosome migration and alignment in laser-ablated embryos (relative to Fig. 2).
(A) Plot of the separation of centrosomes within a CC as a function of time after centrosome separation (2 min, dashed vertical line) in control embryos (grey; *N* = 9 embryos, *n* = 18 cells), ablated cell (green; *N* = 5 embryos, *n* = 5 cells), and non-ablated cell (blue; *N* = 5 embryos, *n* = 5 cells) in laser-ablated embryos between the centrosomes. The dashed line at 17 min indicates the time of NEBD. Error bars, standard error of the mean (s.e.m.).
(B) Plot of the rotation and tilt angles between the CCs and the spindle of the left and right cells at 2-cell stage as a function of time after centrosome separation (2 min, dashed vertical line) in control (*N* = 9 embryos) and ablated embryos between the centrosomes in one cell (*N* = 5 embryos. The dashed line at 17 min indicates the time of NEBD. Error bars, standard error of the mean (s.e.m.).
(C) Plot of the distance between the edge of the nucleus and the centre of the CC as a function of time after centrosome separation (2 min, dashed vertical line) in control embryos (grey; *N* = 6 embryos, *n* = 12 cells), ablated cell (green; *N* = 4 embryos, *n* = 4 cells), and non-ablated cell (blue; *N* = 4 embryos, *n* = 4 cells) in laser-ablated embryos between the centrosomes and the nucleus. The dashed line at 17 min indicates the time of NEBD. Error bars, standard error of the mean (s.e.m.).
(D) Plot of the rotation and tilt angles between the CCs and the spindle of the left and right cells at 2-cell stage as a function of time after centrosome separation (2 min, dashed vertical line) in control (*N* = 9 embryos) and ablated embryos between the centrosomes and the nucleus in one cell (*N* = 4 embryos). The dashed line at 17 min indicates the time of NEBD. Error bars, standard error of the mean (s.e.m.).

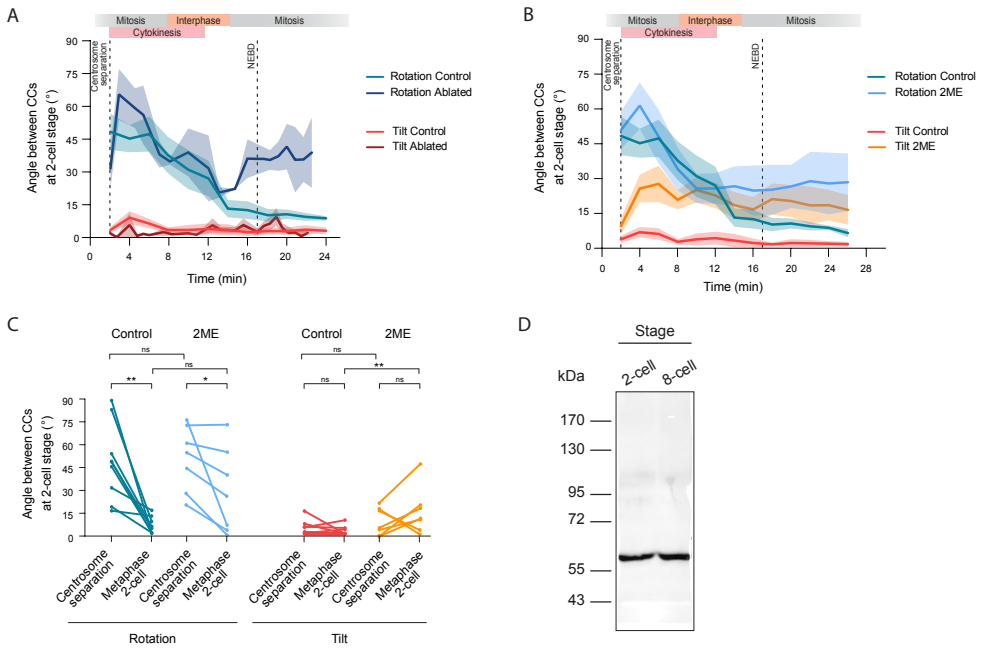

Figure S3: Centrosome alignment relies on forces generated along astral microtubules (relative to Fig. 3).

(A) Plot of the rotation and tilt angles between the CCs and the spindle of the left and right cells at 2-cell stage as a function of time after centrosome separation (2 min, dashed vertical line) in control embryos (*N* = 9 embryos), ablated cell (*N* = 4 embryos, *n* = 4 cells), and non-ablated cell (*N* = 4 embryos, *n* = 4 cells) in laser-ablated embryos. The dashed line at 17 min indicates the time of NEBD. Error bars, standard error of the mean (s.e.m.).

(B) Plot of the rotation and tilt angles between the CCs and the spindle of the left and right cells at 2-cell stage as a function of time after centrosome separation (2 min, dashed vertical line) in control (*N* = 9 embryos) and 2-methoxyestradiol-treated (*N* = 7 embryos). The dashed line at 17 min indicates the time of NEBD. Error bars, standard error of the mean (s.e.m.).

(C) Plot of the initial (Centrosome separation) and final (Metaphase 2-cell) rotation (left) and tilt (right) angles between the left and right CCs and spindle at 2-cell stage in control embryos (*N* = 9 embryos; rotation: paired Wilcoxon test, *P=0.0131; tilt: paired Wilcoxon test, *P=0.0250) and embryos treated with 2ME (*N* = 7 embryos; rotation: paired t test (*P=0.0462); tilt: paired t test (ns – not significant)). Control vs. 2ME rotation angle: one-way ANOVA (***P=0.0005) with Šídák's multiple comparisons test (ns – not significant). Control vs. 2ME tilt angle: Kruskal-Wallis test (*P=0.0186) with Dunn's multiple comparisons test (ns – not significant, **P=0.0040).

(D) Western blot image of the specificity of the ascidian anti-dynactin antibody in ascidian 2-cell and 8-cell stage embryos.

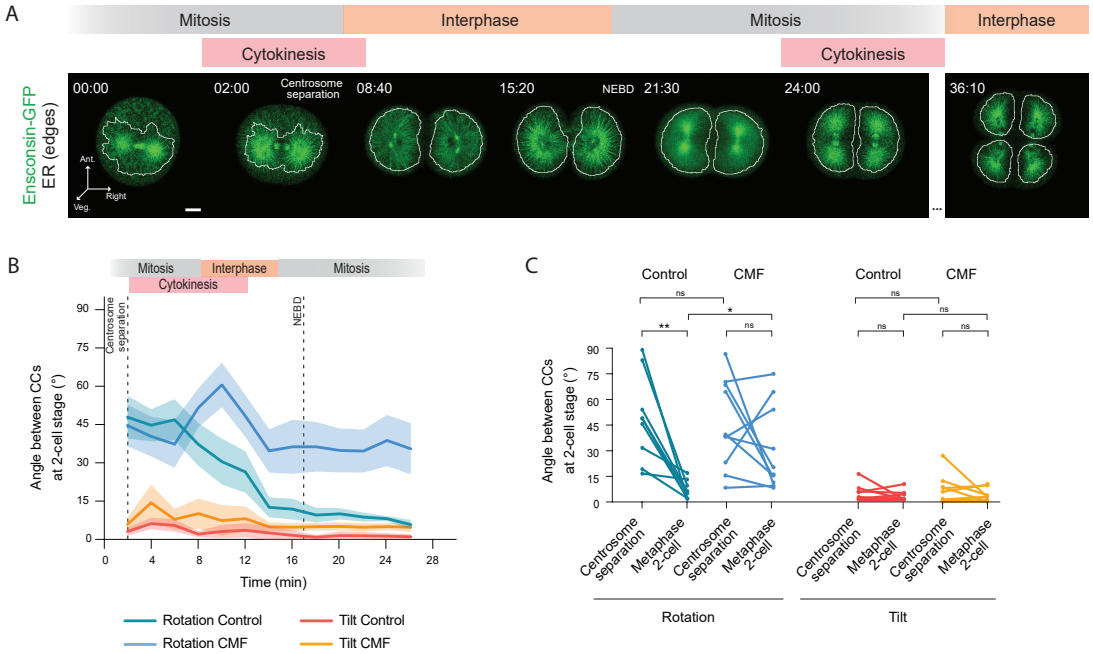

Figure S4: Cytoplasmic pulling controls rotation angles (relative to Fig. 4).

(A) Maximum intensity projections of confocal fluorescent images of microtubules (green) and the edges of the ER cloud around spindles (white) in a representative ascidian embryo from 1-cell stage metaphase to 4-cell stage interphase. Ant. is anterior, Veg. is vegetal, and NEBD is nuclear envelope breakdown. Time is in minutes:seconds. Scale bar, 30 µm.

(B) Plot of the rotation and tilt angles between the CCs and the spindle of the left and right cells at 2-cell stage as a function of time after centrosome separation (2 min, dashed vertical line) in control (*N* = 9 embryos) and embryos in CMF (*N* = 10 embryos). The dashed line at 17 min indicates the time of NEBD. Error bars, standard error of the mean (s.e.m.).

(C) Plot of the initial (Centrosome separation) and final (Metaphase 2-cell) rotation (left) and tilt (right) angles between the left and right CCs and spindle at 2-cell stage in control embryos (*N* = 9 embryos; rotation: paired Wilcoxon test, *P=0.0131; tilt: paired Wilcoxon test, *P=0.0250) and embryos in CMF (*N* = 10 embryos; rotation: paired t test, ns - not significant; tilt: paired t test, ns – not significant). Control vs. CMF rotation angle: one-way ANOVA (***P=0.0010) with Šídák's multiple comparisons test (ns – not significant, *P=0.0431). Control vs. CMF tilt angle: Kruskal-Wallis (ns – not significant) with Dunn's multiple comparisons test ns – not significant).

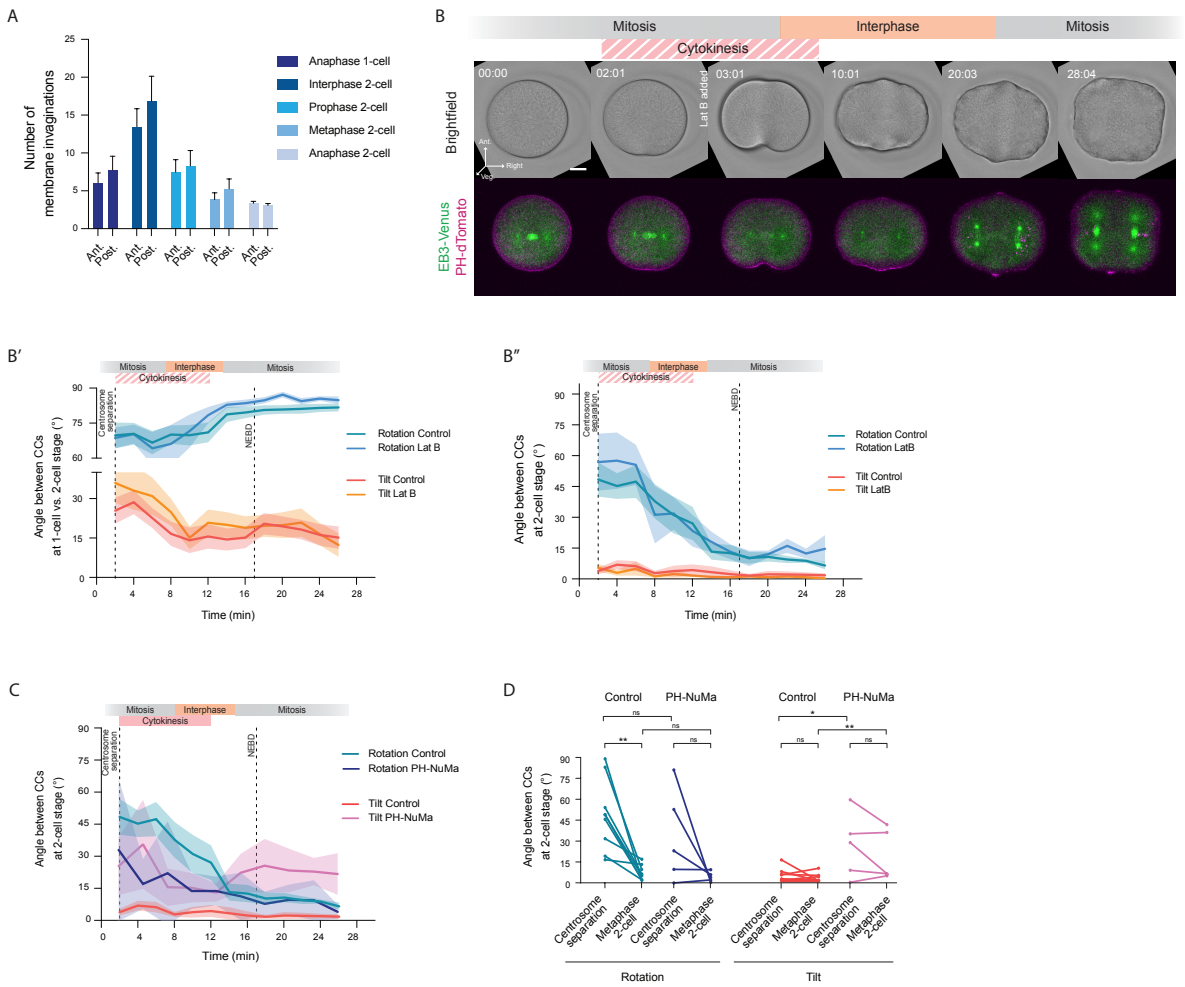

Figure S5: Cortical pulling is increased in the posterior of the ascidian 2-cell stage embryo (relative to Fig. 5).

(A) Bar plot of the average number of membrane invaginations at the anterior (Ant.) and posterior (Post.) sides of the embryo as a function of the cell cycle stage. Data is taken from Fig. 5A''.

(B) Brightfield and confocal fluorescent images of a central z-slice of the plasma membrane (magenta), and maximum intensity projections of centrosomes (green) in a representative ascidian embryo from 1-cell stage metaphase to 2-cell stage metaphase treated with 1 µg/ml Latrunculin B at 1-cell stage anaphase. Ant. is anterior, Veg. is vegetal. Time is in minutes:seconds. Scale bar, 30 µm.

(B') Plot of the rotation and tilt angles between the CCs and the spindle at 2-cell stage and the spindle at 1-cell stage as a function of time after centrosome separation (2 min, dashed vertical line) in control embryos (*N* = 9 embryos, *n* = 18 cells) and Latrunculin B-treated embryos (*N* = 5 embryos, *n* = 10 cells). The dashed line at 17 min indicates the time of NEBD. Error bars, standard error of the mean (s.e.m.).

(B'') Plot of the rotation and tilt angles between the CCs and the spindle of the left and right cells at 2-cell stage as a function of time after centrosome separation (2 min, dashed vertical line) in control (*N* = 9 embryos) and Latrunculin B-treated (*N* = 5 embryos). The dashed line at 17 min indicates the time of NEBD. Error bars, standard error of the mean (s.e.m.).

(C) Plot of the rotation and tilt angles between the CCs and the spindle of the left and right cells at 2-cell stage as a function of time after centrosome separation (2 min, dashed vertical line) in control (*N* = 9 embryos) and embryos expressing PH-NuMA (*N* = 5 embryos, *n* = 10 cells). The dashed line at 17 min indicates the time of NEBD. Error bars, standard error of the mean (s.e.m.).

(D) Plot of the initial (Centrosome separation) and final (Metaphase 2-cell) rotation (left) and tilt (right) angles between the left and right CCs and spindle at 2-cell stage in control embryos (*N* = 9 embryos; rotation: paired Wilcoxon test, *P=0.0131; tilt: paired Wilcoxon test, *P=0.0250) and embryos overexpressing PH-NuMA (*N* = 5 embryos; rotation: paired t test, ns - not significant; tilt: Wilcoxon test, ns – not significant). Control vs. PH-NuMA rotation angle: one-way ANOVA (***P=0.0005) with Šídák's multiple comparisons test (ns – not significant). Control vs. PH-NuMA tilt angle: Kruskal-Wallis test (*P=0.0210) with Dunn's multiple comparisons test (*P=0.0146, ns – not significant).

1139 **MOVIE LEGENDS**

1140 **Movie 1.** Centrosomal complex orientation during the first two cleavages in ascidian embryos, related
1141 to Fig. 1 and S1. Time-lapse brightfield (left panel) and fluorescent confocal video of a representative
1142 ascidian embryo injected with PH-dTomato mRNA (magenta, right panel) and EB3-3xVenus mRNA
1143 (green, right panel) to mark membrane and centrosomes, respectively. Time interval, 2 min.
1144

1145 **Movie 2.** Centrosome and nucleus migration during interphase of the 2-cell stage in ascidian embryos,
1146 related to Fig. 2. Time-lapse fluorescent confocal video of a representative ascidian embryo injected
1147 with EB3-mScarlet mRNA (green), H2B-Venus mRNA (magenta) to mark centrosomes and the DNA,
1148 respectively, and incubated in MitoTracker Deep Red (cyan) to label the mitochondria. Time interval,
1149 16 s.
1150

1151 **Movie 3.** Laser ablation of intercentrosomal microtubules during CC migration at the 2-cell stage of
1152 ascidian embryos, related to Fig. 2 and S2. Time-lapse fluorescent confocal video of a representative
1153 ascidian embryo injected with EB3-mScarlet mRNA (magenta) and Ensconsin-3xGFP mRNA (green) lo
1154 mark centrosomes and microtubules, respectively. Ablation site is indicated by the dashed line. Time
1155 interval, 12.8 s.
1156

1157 **Movie 4.** Laser ablation of microtubules between the CC and the nucleus during CC migration at the 2-
1158 cell stage of ascidian embryos, related to Fig. 2 and S2. Time-lapse fluorescent confocal video of a
1159 representative ascidian embryo injected with H2B-Venus mRNA (magenta) and Ensconsin-dTomato
1160 mRNA (green) lo mark DNA and microtubules, respectively. Ablation site is indicated by the dashed
1161 line. Time interval, 12.8 s.
1162

1163 **Movie 5.** Laser ablation of astral microtubules during CC migration at the 2-cell stage of ascidian
1164 embryos, related to Fig. 3 and S3. Time-lapse fluorescent confocal video of a representative ascidian
1165 embryo injected with EB3-mScarlet mRNA (magenta) and Ensconsin-3xGFP mRNA (green) lo mark
1166 centrosomes and microtubules, respectively. Ablation site is indicated by the dashed line. Time
1167 interval, 12.8 s.
1168

1169 **Movie 6.** Endoplasmic reticulum rearrangement during the first two cleavages in ascidian embryos,
1170 related to Fig. 4 and S4. Time-lapse fluorescent confocal video of a representative ascidian embryo
1171 injected with PH-dTomato mRNA (magenta) and Reticulon-Venus mRNA (grey) to mark the membrane
1172 and endoplasmic reticulum, respectively. Time interval, 110 s.
1173

1174 **Movie 7.** Centrosomal complex orientation during the first two cleavages in ascidian embryos cultured
1175 in Ca^{2+} and Mg^{2+}-free seawater, related to Fig. 4 and S4. Time-lapse brightfield (left panel) and
1176 fluorescent confocal video of a representative ascidian embryo injected with PH-dTomato mRNA
1177 (magenta, right panel) and EB3-3xVenus mRNA (green, right panel) to mark membrane and
1178 centrosomes, respectively. Time interval, 2 min.
1179

1180 **Movie 8.** Cortical pulling assay in control ascidian embryos, related to Fig. 5 and S5. Time-lapse
1181 fluorescent confocal video of a representative ascidian embryo treated with in 1μg/ml Latrunculin B
1182 and injected with H2B-Venus mRNA (magenta) to mark the DNA, and incubated in Cell Mask Orange
1183 to label the plasma membrane (grey). Time interval, 20 s.

1184 **Movie 9.** Cortical pulling assay in ascidian embryos expressing PH-NuMA, related to Fig. 5 and S5. Time-
1185 lapse fluorescent confocal video of a representative ascidian embryo treated with in 1μg/ml
1186 Latrunculin B and incubated in Cell Mask Orange to label the plasma membrane (grey, left panel) and
1187 injected with PH-NuMA-Venus mRNA (magenta, right panel) to mark exogenous cortical NuMA. Time
1188 interval, 16 s.
1189
1190 **Movie 10.** Centrosomal complex orientation during the first two cleavages in ascidian embryos
1191 expressing PH-NuMA to increase cortical pulling, related to Fig. 5 and S5. Time-lapse brightfield (left
1192 panel) and fluorescent confocal video of a representative ascidian embryo injected with PH-NuMA-
1193 Venus mRNA (magenta, right panel) and EB3-mScarlet3 (green, right panel) to mark exogenous cortical
1194 NuMA and centrosomes, respectively. Time interval, 2 min.
1195